

Angular momentum properties of haloes and their baryon content in the *Illustris* simulation

Jolanta Zjupa^{1,2*} and Volker Springel^{1,3}

¹*Heidelberger Institut für Theoretische Studien, Schloss-Wolfsbrunnenweg 35, 69118 Heidelberg, Germany*

²*Institut für Theoretische Physik, Philosophenweg 16, 69120 Heidelberg, Germany*

³*Zentrum für Astronomie der Universität Heidelberg, Astronomisches Recheninstitut, Mönchhofstr. 12-14, 69120 Heidelberg, Germany*

Accepted, Received; in original form

ABSTRACT

The angular momentum properties of virialised dark matter haloes have been measured with good statistics in collisionless N -body simulations, but an equally accurate analysis of the baryonic spin is still missing. We employ the *Illustris* simulation suite, one of the first simulations of galaxy formation with full hydrodynamics that produces a realistic galaxy population in a sizeable volume, to quantify the baryonic spin properties for more than $\sim 320,000$ haloes. We first compare the systematic differences between different spin parameter and halo definitions, and the impact of sample selection criteria on the derived properties. We confirm that dark matter only haloes exhibit a close to self-similar spin distribution in mass and redshift of lognormal form. However, the physics of galaxy formation radically changes the baryonic spin distribution. While the dark matter component remains largely unaffected, strong trends with mass and redshift appear for the spin of diffuse gas and the formed stellar component. With time the baryons staying bound to the halo develop a misalignment of their spin vector with respect to dark matter, and increase their specific angular momentum by a factor of ~ 1.3 in the non-radiative case and ~ 1.8 in the full physics setup at $z = 0$. We show that this enhancement in baryonic spin can be explained by the combined effect of specific angular momentum transfer from dark matter onto gas during mergers and from feedback expelling low specific angular momentum gas from the halo. Our results challenge certain models for spin evolution and underline the significant changes induced by baryonic physics in the structure of haloes.

Key words: methods: numerical – cosmology: theory – galaxies: formation and evolution – galaxies: angular momentum.

1 INTRODUCTION

The origin of the angular momentum of galaxies is an important question in cosmic structure formation, as the spin directly determines the size of rotationally supported objects such as disk galaxies. In the now well established standard paradigm of the Λ CDM concordance cosmology, primordial dark matter density perturbations seeded in an inflationary epoch grow with time due to gravitational instability. Eventually, they decouple from the background expansion, turn around and collapse to form virialised structures. This happens first for small mass systems, which then hierarchically merge into bigger structures (Blumenthal et al. 1984; Davis et al. 1985). The baryons collected within haloes cool out and form galaxies at their centres, giving rise to a hierar-

chical galaxy formation process (White & Rees 1978). If the baryons have a non-vanishing specific angular momentum, it should be preserved in the radiative cooling process, such that the gas settles into a rotationally supported disk that forms inside out (Fall & Efstathiou 1980; Mo, Mao & White 1998), with a size directly related to the magnitude of the spin.

It is thus important to clarify the amount of angular momentum imparted on haloes and on the baryons they contain. Generally, gravitationally self-bound structures gain their initial angular momentum from interactions with the surrounding gravitational tidal field (Hoyle 1949). This in particular makes it possible that haloes acquire substantial non-vanishing angular momentum even though the gravitational potential is irrotational in character. The amount of angular momentum contained in a galaxy as well as the growth rate in the linear regime was first calculated by Peebles (1969). Doroshkevich (1970) pointed out that this par-

* E-mail: jolanta.zjupa@h-its.org

ticular growth rate is a consequence of the imposed spherical symmetry and carried out a calculation predicting the angular momentum to grow linearly with time before non-linear effects start to play a significant role. These results were confirmed by early collisionless dark matter only N-body simulations by White (1984) and Barnes & Efstathiou (1987), and form the basis of the so-called tidal torque theory, which describes the acquisition of angular momentum for dark matter haloes (see also Schäfer & Merkel 2012).

However, once the subsequent evolution of haloes enters the non-linear regime, simple tidal torque theory breaks down, as haloes cannot be regarded any more as isolated objects. Instead, they undergo multiple minor and major mergers. Analytic and semi-analytic models for the acquisition of angular momentum from the orbital angular momentum of infalling mergers (e.g. Vitvitska et al. 2002; Maller, Dekel & Somerville 2002; Maller & Dekel 2002) can successfully extend tidal torque theory and reproduce the spin parameter distribution of haloes as well as the distribution of specific angular momentum inside haloes at $z = 0$. However, such analytic descriptions rely on simplifying and ultimately uncertain assumptions. On the other hand, the acquisition of angular momentum through non-linear processes such as mergers is followed faithfully in numerical simulations, making them a particularly powerful approach to study this problem.

This has motivated numerous analysis of the angular momentum properties of simulated dark matter only haloes. Avila-Reese et al. (2005) studied the dependence of halo spin on environment, Macciò et al. (2007) investigated the correlation of halo spin with mass and concentration, and Macciò, Dutton & van den Bosch (2008) extended this analysis to the dependence of halo spin on mass and cosmology. Bett et al. (2007) have derived spin parameters for $\sim 1.5 \times 10^6$ dark matter only haloes from the Millennium simulation (Springel et al. 2005) and accurately quantified the spin parameter distribution with the highest statistical power so far. Bullock et al. (2001) extended the analysis to the distribution of specific angular momentum within haloes and found a universal angular momentum profile within the virial radius. The most important result from these studies has been the finding of a nearly universal spin parameter distribution of approximately lognormal form. A closer look at some of the results reported in the literature however also reveals some small quantitative differences, as we will discuss in detail in this paper.

When it comes to baryonic processes, even more interesting differences appear. Although the dynamics of the galaxy and the dark matter are to a large extent determined by the common gravitational potential of the dark matter halo (Rubin & Ford 1970), so-called feedback processes play an important role in shaping galaxy formation and evolution, primarily through changing the gas dynamics. However, even in absence of feedback mechanisms, it is not trivially possible to extrapolate from dark matter onto baryonic spin properties. This can be already seen in early results from non-radiative hydrodynamical simulations. In particular, van den Bosch et al. (2002) showed in their non-radiative hydrodynamical simulation that even though the ‘initial’ spin distributions of dark matter and the gas component of haloes are indistinguishable, there is a substantial misalignment between dark matter and the gas component

at $z = 3$, with a significant fraction of the gas being counter-rotating. The median misalignment angle reported is $\sim 30^\circ$. Chen, Jing & Yoshikawa (2003), Sharma & Steinmetz (2005), and Gottlöber & Yepes (2007) extended this analysis to $z = 0$ and found a relative enhancement of the gas to dark matter spin parameter of 1.19, 1.44, and 1.39, respectively. However, until recently the analysis of the spin was largely restricted to non-radiative simulations, as full physics simulations of galaxy formation were simply too costly and did not produce realistic galaxy populations.

The impact of baryons onto dark matter in models where star formation and feedback is taken into account was first studied by Bett et al. (2010), who employed a sample of 67 haloes and their dark matter only counterparts and found an increase of the specific angular momentum of dark matter in the inner regions of haloes in the presence of baryons. Bryan et al. (2013) looked at larger statistical samples of $\gtrsim 3000$ haloes taken from the OWLS simulations and confirmed this finding.

First results on the angular momentum properties of the stellar component of galaxies from a realistic galaxy population taken from the *Illustris* simulation were obtained by Genel et al. (2015) who showed a correlation between galaxy type and specific angular momentum. This correlation was further confirmed by Zavala et al. (2016) using the EAGLE simulation. Furthermore, Genel et al. (2015) observed that galactic winds enhance the spin of stars compared to the dark matter, and that AGN feedback counteracts this effect by damping this enhancement, as also indirectly observed by Bryan et al. (2013). Baldi et al. (2016) studied rotational support in clusters and found, based on their sample of 258 both relaxed and unrelaxed clusters from the MUSIC simulation, little dependence of the gas spin parameter on the implemented baryonic physics.

Teklu et al. (2015) and Rodriguez-Gomez et al. (2016) further investigated the correlation between galaxies and their host haloes. Employing a sample of 622 haloes, with no restriction on their dynamical state, 64 of which host spiral galaxies and 110 ellipticals, Teklu et al. (2015) found that haloes hosting spiral galaxies exhibit on average higher spins, and haloes hosting elliptical on average lower spins. This trend was previously only weakly observed by Sales et al. (2012), who found little evidence for galaxy morphology of 100 Milky Way sized galaxies from the GIMIC Simulation to be connected to halo spin and merging history, and argued that galaxy morphology is rather determined by the misalignment of angular momentum inside the galaxy and its host halo at turnaround. Rodriguez-Gomez et al. (2016) showed that the correlation between galaxy morphology and host halo spin is a strong function of halo mass, as in more massive haloes mergers play an increasingly important role in perturbing the gas distribution of the central galaxy. Zavala et al. (2016) followed the time evolution of the specific angular momentum of different halo components and presented different evolution scenarios for the baryonic component, and their connection to the morphology of the galaxy forming at the halo centre.

In this paper we investigate how the dynamics of the baryonic and the dark matter component of haloes are influenced by feedback processes for a large statistical sample of $\sim 320,000$ haloes from the *Illustris* simulation. Our analysis focuses on the systematic properties of the angular momen-

tum content of whole haloes, and how it changes relative to dark matter only simulations when baryonic physics is included.

This paper is structured as follows. We begin in Section 2 with a brief description of our simulation methodology and details on our halo identification and sample selection. We furthermore discuss in detail the effects of sample selection criteria and adopted spin parameter definition on the spin statistics. We then present results for the angular momentum statistics of dark matter only haloes in Section 3, followed by results from non-radiative baryonic simulations in Section 4 and from the full physics *Illustris* simulation in Section 5. In each of these sections we also examine the robustness of our results with respect to resolution, the redshift evolution of the spin statistics, and the dependence of the spin properties on halo mass. Section 5 contains a discussion of the effect of feedback onto the baryonic and dark matter spin properties and highlights the main mechanisms responsible for a substantially enhanced spin of the gas component. We give a discussion and our conclusions in Section 6, and summarise extensions to the *Illustris* group catalogue in an Appendix.

2 METHODOLOGY

2.1 The *Illustris* simulation suite

The *Illustris* simulation suite consists of a set of cosmological hydrodynamical simulations of a $75 h^{-1}$ Mpc wide periodic cosmological box carried out with the moving mesh code AREPO (Springel 2010a). Initial Conditions were generated at $z = 127$ and evolved to $z = 0$ with 1820^3 dark matter particles and 1820^3 initial gas cells in the highest resolution run, achieving a mass resolution of $6.26 \times 10^6 M_\odot$ in dark matter and $1.26 \times 10^6 M_\odot$ in baryonic matter. To investigate numerical convergence, runs with a reduced number of initial dark matter particles and gas cells were performed as well. Furthermore, for every resolution the simulations were carried out with three different physical setups, a dark matter only, a non-radiative, and a full galaxy formation physics setup. An overview of the different *Illustris* simulations and their principal parameters is given in Tab. 1.

In the dark matter only simulations, all mass is treated as collisionless dark matter, while the non-radiative setup follows in addition the hydrodynamics of the gas but ignores radiative cooling and star formation. The full physics simulation includes these and further processes related to galaxy formation through a model described in full in Vogelsberger et al. (2013). In brief, unresolved physics of the interstellar medium is modelled in a subgrid fashion, where star formation is regulated by a pressure model that accounts for supernova feedback in the interstellar medium. This model also includes chemical enrichment through explicit tracking of 9 elements. Furthermore, black hole growth through gas accretion and associated energy feedback processes are included. The *Illustris* simulation is one of the first cosmological hydrodynamical simulations of galaxy formation that produces a realistic population of galaxies at $z = 0$. Other recent projects that show similar successes are the EAGLE simulation (Schaye et al. 2015) and the Horizon-AGN simulation (Dubois et al. 2016).

Simulation	Simulation type	dm	gas
Illustris-1	full physics hydro.	1820^3	1820^3
Illustris-2	full physics hydro.	910^3	910^3
Illustris-3	full physics hydro.	455^3	455^3
Illustris-2-NR	non-radiative hydro.	910^3	910^3
Illustris-3-NR	non-radiative hydro.	455^3	455^3
Illustris-1-Dark	collisionless dm only	1820^3	-
Illustris-2-Dark	collisionless dm only	910^3	-
Illustris-3-Dark	collisionless dm only	455^3	-

Table 1. *Illustris* simulation suite: listed are the symbolic name, the physics included, the number of initial dark matter particles, and the number of initial gas cells for every simulation.

The galaxy formation physics model of *Illustris* simultaneously reproduces with reasonable accuracy a number of observed small-scale properties, such as galaxy stellar masses and morphologies, as well as large-scale properties, such as the metal abundance in neutral hydrogen absorption systems, or the radial distribution of galaxies in galaxy clusters (e.g. Vogelsberger et al. 2014). It is thus interesting to examine the spin distribution of the baryons in such a calculation, which can be viewed as representing one of the most realistic predictions for the large-scale dynamics of the baryons available thus far. This motivation is further strengthened by the use of the AREPO code for the simulation, which follows the gas mass in a quasi-Lagrangian form by means of a fully adaptive mesh that moves with the flow. This approach avoids classical disadvantages of Cartesian adaptive mesh refinement (AMR) codes, such as the occurrence of preferred spin directions along the coordinate axes (e.g. Hahn, Teyssier & Carollo 2010). Simultaneously, it eliminates traditional problems of smoothed particle hydrodynamics (SPH), such as relatively high numerical noise and the need for an artificial viscosity (Springel 2010b). We thus expect that AREPO follows the hydrodynamics more accurately than competing numerical approaches, making its predictions for the spin of the baryonic component of haloes all the more interesting.

However, we note that like any other numerical code, AREPO is constantly improved further. In particular, Pakmor et al. (2016) has recently proposed changes in the gradient estimation as well as time integration of the code that improve its accuracy and convergence order in certain situations. The *Illustris* suite analysed here was carried out with a version of the code that did not include these improvements, but as Pakmor et al. (2016) show, they do not affect the results of cosmological simulations of galaxy formation.

2.2 Measurement of halo properties through an extension of SUBFIND

During the *Illustris* simulation runs, the group finders FOF and SUBFIND (Springel et al. 2001) were applied on the fly, determining a set of basic halo and subhalo properties, as described in detail in the public data release of *Illustris* (Nelson et al. 2015). However, the spin properties we want to analyse here, as well as information about the binding energy of haloes were not part of these properties. Unfortunately, simply computing additional halo properties post-

hoc is technically complicated. While the *Illustris* data is stored such that the particle/cell data comprising individual gravitationally bound subhaloes can be retrieved relatively easily despite the large simulation size, this is not readily possible for the particles/cells making up an object defined by its spherical overdensity radius R_{200} . Also, computing the binding energy of haloes that consist of a large number or resolution elements (regularly in excess of 10^6 elements) becomes computationally costly unless sophisticated algorithms are employed.

In order to efficiently measure further halo and subhalo properties for *Illustris*, we have therefore developed an extension of AREPO’s group finders that allows the parallel processing of an already existing group catalogue. The membership of individual resolution elements to groups, subhaloes and spherical overdensity haloes is kept exactly as in the existing group catalogue, allowing additional properties of haloes to be measured. The results are then simply added as further fields to the catalogue. A full list of the newly available halo and subhalo properties in the extended group catalogue can be found in the Appendix¹. Thanks to the parallel tree solver for gravity in AREPO, one of the quantities we can calculate in this way efficiently is the exact gravitational binding energy of haloes (including spherical overdensity objects), something that has often been only determined in an approximate way in previous analysis of halo spin. The code extension of FOF/SUBFIND is written such that it can run both as a postprocessing option to augment existing catalogues, or as part of the regular group finding, either on-the-fly or in postprocessing. We also note that since the group catalogue is stored in the convenient HDF5 format, the I/O routines of existing analysis code using the group catalogue does not have to be adjusted or changed after the group catalogue has been extended.

For definiteness, we briefly summarise the group definitions adopted by *Illustris*, which we also employ in the following. Friends-of-friends (FOF) groups are determined for dark matter particles as a set of equivalence classes, where any pair of two particles is in the same group if their distance is smaller than a prescribed linking length. For the linking length we adopt the standard value of 0.2 times the mean particle spacing, $l_{\text{mean}} = (m_{\text{dm}}/\rho_{\text{dm}})^{1/3}$, where m_{dm} is the dark matter particle mass, and ρ_{dm} is the mean dark matter density. Baryonic particles (stars and black holes) and gaseous cells, if present, are then assigned in a second step to the same halo as their closest dark matter particle. Any group constructed in this way corresponds to what we from now on call a FOF-halo. While all groups with at least 32 particles/cells are stored for the *Illustris* simulation, for our analysis we will typically impose a considerably higher minimum particle number in order to prevent numerical noise and possible biases from poorly resolved haloes.

Each FOF-halo is then decomposed by SUBFIND into a set of gravitationally self-bound subhaloes, based on the algorithm described in Springel et al. (2001). To this end, the total mass density at each point is estimated by an adaptive kernel estimation. The resulting density field is then processed with an excursion set technique that finds locally

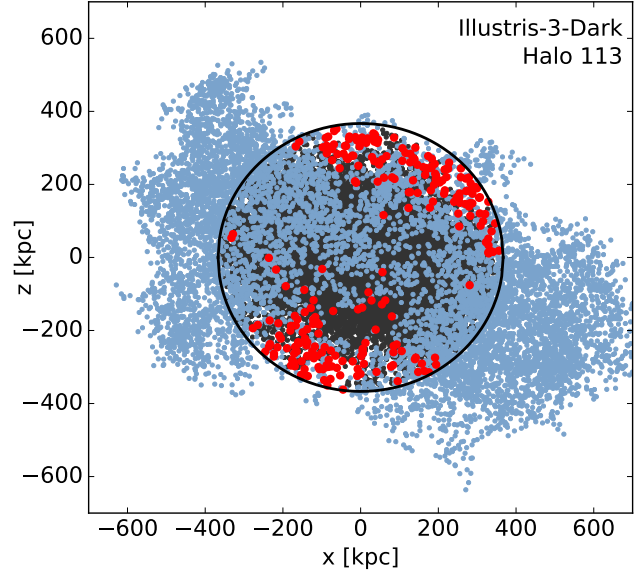


Figure 1. Particles making up a randomly selected dark matter halo from Illustris-3-Dark. The black circle indicates R_{200} , FOF-halo dark matter particles inside R_{200} are shown in *grey*, FOF-halo dark matter particles outside R_{200} are shown in *blue*, dark matter particles part of the SO-halo definition but not the FOF-halo are shown as *big red dots*. This demonstrates the general fact that FOF-haloes are typically more extended and more massive than their SO-halo counterparts. The number of particles that are part of the SO-halo but not the FOF-halo is usually relatively small, such that SO-haloes can be regarded as the inner regions of FOF-haloes.

overdense candidate substructures. Each of these overdensities is then subjected to a gravitational unbinding procedure, keeping only the bound part as a genuine substructure. Every resolution element can only be member of one subhalo, and the remaining bound part of the halo, after all smaller substructures have been removed, is called the background subhalo. For each subhalo the particle/cell with the smallest gravitational potential is adopted as its centre.

Finally, around the centre of each background subhalo, which corresponds to the point with the minimum gravitational potential of the underlying FOF-halo, we determine spherical overdensity (SO) groups. In this approach, one finds a spherical region around a given point *in the full particle/cell set* that encloses a certain overdensity with respect to the background density. We will generally employ an overdensity of 200 with respect to the critical density, and denote the corresponding radius and mass of the spherical region as R_{200} and M_{200} , respectively. In Fig. 1 we depict a typical halo to illustrate the different halo definitions and highlight some of the implications for halo geometry and the calculation of halo properties.

2.3 Halo sample selection

For our analysis, we select all sufficiently well-resolved haloes that appear to be reasonably relaxed systems. To avoid numerical biases due to resolution effects, following the detailed resolution study of Bett et al. (2007), we exclude all haloes resolved by less than 300 dark matter particles from

¹ They will be added to the public data release of *Illustris* described by Nelson et al. (2015) upon publication of this paper.

our FOF-halo and SO-halo samples.² We also exclude all haloes that have no gravitationally self-bound component identified by SUBFIND, as these are not haloes in a physical sense.

Furthermore, we want to study only haloes close to virial equilibrium, in order to avoid, for example, situations where the angular momentum content is dominated by the contribution of the orbital angular momentum of mergers. To this end we calculate the virial ratio,

$$q = \frac{2E_{\text{kin}}}{E_{\text{pot}}} + 1, \quad (1)$$

both for our FOF- and SO-halo samples. The total kinetic energy in Eq. (1) represents the sum of the bulk kinetic energy of the halo particles/cells and the thermal energy of the gas, if present. In calculating the virial ratio according to Eq. (1) we ignore the surface pressure term, which appears in the virial theorem for non-isolated systems (Shapiro et al. 2004) and represents the pressure exerted on the halo by infalling matter. In our approach it is sufficient to calculate the virial ratio in such an approximative way, as we only employ it to filter out systems that have a huge surplus of kinetic energy.

For an isolated structure in equilibrium the expected virial ratio based on the virial theorem is $q = 0$. In Fig. 2 we show the distribution of virial ratios of our FOF-halo samples from Illustris-1-Dark and from Illustris-1 against halo mass. In this effectively two-dimensional histogram, the individual mass bins have been independently normalised to take out the variation of halo abundance with mass. The virial equilibrium expectation is denoted by the horizontal blue line. Haloes with positive q -values are dominated by potential energy, haloes with negative q -values are dominated by kinetic energy. We dismiss all haloes with $q < -1$ from our halo sample, corresponding to haloes having more than twice as much kinetic energy as expected from virial equilibrium. Those objects are often undergoing significant mergers, which can produce highly negative q -values.

Both simulations show that the average virial ratio of haloes decreases with halo mass. This reflects the fact that less massive haloes form on average at higher redshifts and thus have more time to virialise by $z = 0$, whereas more massive haloes are still in the process of collapsing and virialising at $z = 0$, which is additionally slowed down by further growth through accretion. More massive haloes are also known to be more elongated on average, consistent with their younger age and more active infall region.

In Fig. 3 we show how the virial ratio distributions of the FOF-halo samples of Illustris-1-Dark and Illustris-1 evolve with time. As there are many more low mass haloes than high mass haloes, the distributions are dominated by the mass scale just above the enforced threshold of 300 dark matter particles. Black dots indicate the median virial ratio at the displayed redshifts. For both simulations the contribution of kinetic energy is enhanced at high redshift, pushing the bulk of the haloes further away from the equilibrium value, reflecting their ongoing rapid growth and young age. The virial ratio distribution $P(q)$ normalised to the

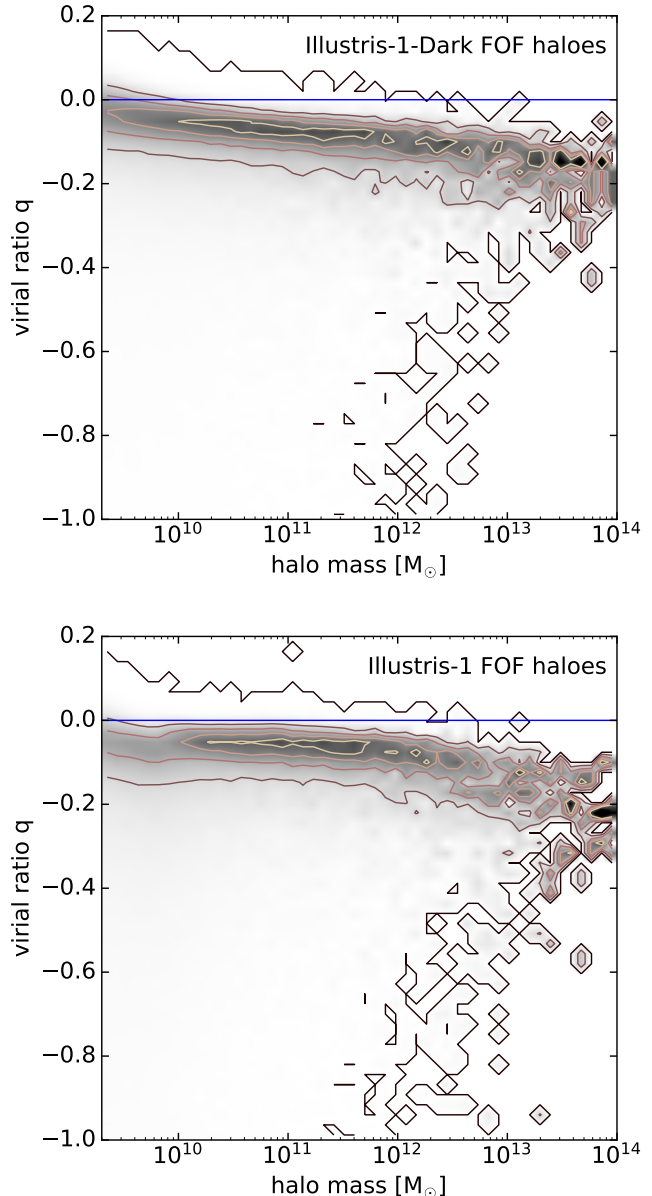


Figure 2. Distribution of the virial ratio q of the FOF-halo sample from Illustris-1-Dark and Illustris-1 normalised in every mass bin. The grey shading ranges from a fraction of 0 to 0.2 of all haloes in a mass bin having a given q -value. Contours are drawn at constant fractions of 0, 0.05, 0.1, 0.15, and 0.2, respectively. The blue line denotes virial equilibrium. Negative virial ratios correspond to haloes being dominated by kinetic energy. In case of massive haloes this surplus of kinetic energy is due to the halo not being fully collapsed yet. The tail to extreme negative values for less massive haloes is due to mergers.

total number of haloes as well as bin size thus peaks at low q -values at high redshift and then progressively shifts towards $q = 0$ with decreasing redshift, corresponding to the halo sample becoming more virialised with cosmic time. Our SO-halo sample shows qualitatively the same behaviour. This reflects the fact that cosmic structures are hardly ever in perfect virial equilibrium, but rather in a slowly evolving quasi-equilibrium. However, we caution that the trends

² Note that this imposes a somewhat higher minimum halo mass in the *Illustris* simulations including baryons compared to dark matter only.

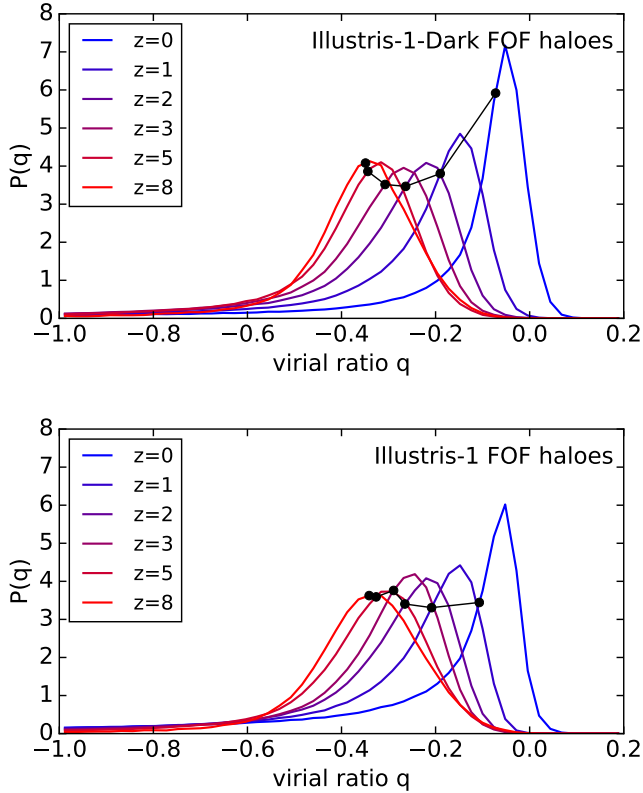


Figure 3. Change of the virial ratio distribution of FOF-haloes as a function of redshift, both for Illustris-1-Dark (top panel) and Illustris-1 (bottom panel). Black dots indicate the median virial ratio at every redshift. With decreasing redshift, the FOF-halo sample becomes ever more relaxed, with the median virial ratio shifting continuously towards zero and hence to the expectation value for perfectly relaxed isolated systems.

displayed here were derived neglecting the pressure surface term, which is smaller both for more massive and younger haloes, as both are undergoing more accretion. A higher absolute value of the negative pressure surface term results in the trends being weaker than shown here. Nevertheless, when comparing halo samples at different redshifts, one thus has to bear in mind that the samples will typically exhibit different degrees of relaxation.

Furthermore, we want to emphasise that there is no universally accepted standard definition of what constitutes a well-resolved, quasi-equilibrium structure in cosmological simulations. Besides a different minimum number of particles and different virial ratio cuts, also criteria such as the offset between the centre of mass and the potential minimum, the abundance of dark matter substructures (Macciò et al. 2007), or the mass fraction in substructures not being bound to the main potential (Neto et al. 2007) have been employed in the literature to discriminate between relaxed and unrelaxed haloes. The effect of the different sample selection criteria on the final values of the derived properties, such as the spin parameter distribution and median spin parameter value for dark matter only haloes, has not been systematically investigated yet.

However, as we will show later, the inferred spin distribution of haloes is equally sensitive to the halo and spin

parameter definitions as on the exact set of selection criteria for the halo sample. Which halo definition is considered to be more physical or useful is largely a matter of convention. In this paper, we will present results for both the FOF-halo and SO-halo sample, which can be regarded as the two most important limiting cases. The systematic differences arising from the spin parameter definition are investigated in the next section.

2.4 Spin parameter definitions

The angular momentum content and degree of rotational support of structures with different mass and spatial extent can be quantified and compared by means of a suitably defined dimensionless spin parameter λ . Its classic definition,

$$\lambda_{\text{P}} = j_{\text{sp}} \frac{E_{\text{tot}}^{1/2}}{GM_{\text{tot}}^{3/2}}, \quad (2)$$

goes back to Peebles (1969). Here $j_{\text{sp}} = J/M$ gives the magnitude of the specific angular momentum per unit mass of the material in question. It is multiplied by a factor composed of the total mass of the system M_{tot} , the gravitational constant G , and the absolute value of the total energy, $E_{\text{tot}} = |E_{\text{kin}} + E_{\text{pot}}|$, where the kinetic energy is again the sum of the bulk kinetic energy of the halo particles/cells and the thermal energy of the gas. This multiplicative factor expresses the specific angular momentum $j_{\text{sp}} = |\mathbf{j}_{\text{sp}}|$ in dimensionless form.

Note that the specific angular momentum can be calculated for any subset of the system. If the set is composed of N mass elements, with the i -th computational element having mass m_i , distance from the halo centre \mathbf{r}_i , and velocity \mathbf{v}_i with respect to the centre of mass velocity of the halo, the specific angular momentum is given as

$$\mathbf{j}_{\text{sp}} = \frac{\mathbf{J}}{M} = \frac{1}{M} \sum_{i=1}^N m_i \mathbf{r}_i \times \mathbf{v}_i, \quad (3)$$

with mass $M = \sum_i m_i$ of the subset. In a simulation including baryons, the most interesting subsets include the dark matter, the gas, and the stellar component of the halo. If the subset consists of the whole halo, one arrives at $M = M_{\text{tot}}$, and the definition of the spin parameter corresponds to that of Peebles (1969).

Early analytic studies of structure formation of dissipationless haloes in the Einstein-de Sitter limit were able to estimate the average value of the spin parameter imparted on density perturbations by gravitational tidal torques. Applying different approaches and simplifying assumptions Heavens & Peacock (1988) found a value of $\lambda_{\text{P}} \approx 0.05$, Ryden (1988) a value of $\lambda_{\text{P}} \approx 0.09$, and Steinmetz & Bartelmann (1995) arrived at $\lambda_{\text{P}} \approx 0.07$. Early dark matter only simulations of the Einstein-de Sitter universe measured systematically lower Peebles spin parameters than suggested by some of these analytic studies. Barnes & Efstathiou (1987) and Warren et al. (1992) quote a value of $\lambda_{\text{P}} \approx 0.05$, and Cole & Lacey (1996) found $\lambda_{\text{P}} \approx 0.04$ in their simulations.

The Peebles spin parameter definition has however an important practical drawback. The potential binding energy E_{pot} of a self-bound structure is needed to determine its total energy. This can be computationally expensive to measure accurately for an N-body halo, especially if its particle

number is large. To avoid this complication, Bullock et al. (2001) proposed an alternative definition of the spin parameter,

$$\lambda_B = \frac{j_{\text{sp}}}{\sqrt{2}R_{200}v_{200}}. \quad (4)$$

In this definition, R_{200} and v_{200} are the virial radius and the circular velocity at the virial radius of the halo, which can be viewed as characteristic length and velocity scales of the object in question, and are here used to express the specific angular momentum in dimensionless form. The prefactor of $1/\sqrt{2}$ is introduced to make this definition of the spin parameter yield the same value as the definition of Peebles (1969) for the density distribution of a singular isothermal sphere truncated at R_{200} , and where all particles are put on circular orbits. Mo, Mao & White (1998) furthermore argue that the two spin parameter definitions are related by $\lambda_P = f(c)^{1/2}\lambda_B$ for NFW-haloes, where $f(c)$ is a function depending only on the concentration c of the halo.

The Bullock definition has been popular and is widely employed in the literature, as it is easy to calculate and does not require the knowledge of the potential energy of a halo, which is often estimated only approximately to reduce the computational cost. Macciò et al. (2007) quote a median Bullock spin of $\lambda_B \approx 0.030$ for their relaxed halo sample, and Avila-Reese et al. (2005) report a value of $\lambda_B \approx 0.033$. The values found for the Bullock spin parameter are all systematically lower than spin parameters derived with the Peebles spin parameter definition. This is in agreement with Bullock et al. (2001) who calculated the median spin parameter according to their new definition and the classic definition by Peebles (1969) for the same SO-halo sample and found values of $\lambda_B \approx 0.035$ and $\lambda_P \approx 0.042$, respectively. Thus, although $f(c)$ is close to unity and the Peebles and Bullock spin parameters are ‘approximately’ equal, there are clearly systematic differences that have to be taken into account when performing precision measurements.

To highlight these systematic differences between the Peebles and Bullock spin parameter definitions, we calculate the spin according to both definitions for our FOF- and SO-halo samples. The total energy needed for the Peebles spin definition is given by $E_{\text{tot}} = |E_{\text{kin}} + E_{\text{pot}}|$, where we calculate the potential energy with high precision employing the parallel gravity tree solver, as described in Section 2.2, and the kinetic energy³ is again the sum of the bulk kinetic energy of the halo particles/cells and the thermal energy of the gas. To calculate the Bullock spin parameter we express the virial velocity $v_{200} = 10H(z)R_{200}$ via the virial radius R_{200} , which is determined for SO-haloes by SUBFIND and contained in the group catalogue. In the case of FOF-haloes, we use the FOF-halo mass M_{FOF} to estimate an equivalent virial radius $R_{200,\text{FOF}} = (GM_{\text{FOF}}/100H^2)^{1/3}$, which corresponds to the assumption that the FOF-halo has all of its mass contained within a sphere of overdensity 200 relative to the critical density. This is a very crude estimate and highlights the limitation of the Bullock spin parameter definition being designed for spherically symmetric haloes,

³ Note that in our extended group catalogue E_{kin} contains only the kinetic energy due to the particle and cell velocities. The thermal energy of the gas is stored in E_{thr} and has to be added to E_{kin} to obtain the total physical kinetic energy.

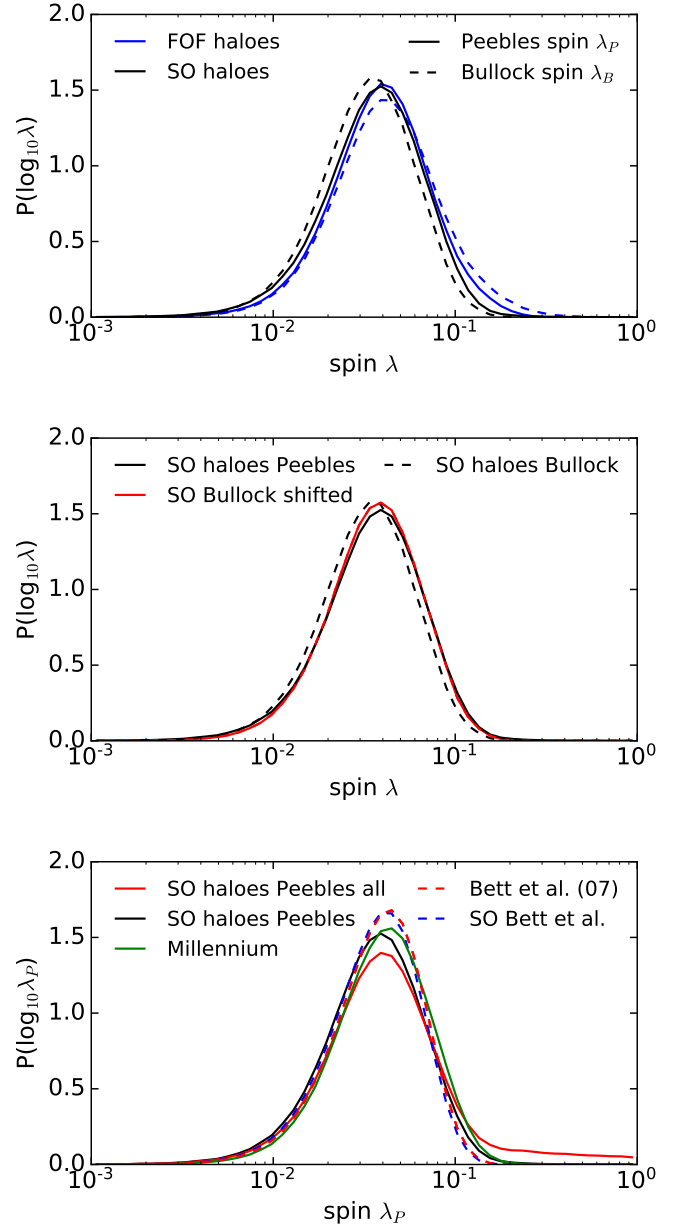


Figure 4. *Upper panel:* Comparison of the Peebles and Bullock spin parameter distributions derived from Illustris-1-Dark for dark matter only FOF- and SO-haloes. The Peebles spin definition yields consistent results for the different halo definitions. *Middle panel:* Comparing the spin values derived with the Bullock spin definition for SO-haloes to the Peebles values, ignoring the concentration dependence but taking into account a constant conversion factor of 1.1. *Lower panel:* Comparison of our SO-halo Peebles distribution from Illustris-1-Dark (black solid) and the Millennium Simulation (green solid) to the Peebles distribution from Bett et al. (2007) derived for their cleaned halo sample (red dashed) and SO-halo sample (blue dashed). The red solid line shows the resulting spin distribution from Illustris-1-Dark when all restrictions on the dynamic state of haloes are abandoned. Different sample selection criteria thus explain the observed differences in the spin distributions and their effect has to be borne in mind when aiming for precision measurements.

because only then the values measured operationally for the characteristic radius R_{200} and velocity v_{200} can be expected to make sense. The Bullock spin parameter definition has no built in mechanism to account for the complicated geometry of FOF-haloes.

In the upper panel of Fig. 4, we show the spin parameter distributions derived with the Peebles and Bullock spin parameter definitions applied to our FOF- and SO-halo samples, which comprise $\sim 400,000$ and $\sim 360,000$ objects, respectively. The distributions are derived by binning the haloes in the given spin parameter range in 50 equidistant logarithmic bins and normalising the number of haloes per bin by the total number of haloes and the logarithmic bin size, such that $\int_{-\infty}^{\infty} P(\log_{10}\lambda) d\log_{10}\lambda = 1$. With this normalisation the shown distribution is independent of the chosen bin size and the total number of bins.

The Peebles spin parameter definition yields almost the same distribution for FOF- and SO-haloes with median spin parameters of $\lambda_{P,FOF} = 0.0391$ and $\lambda_{P,SO} = 0.0365$ for the FOF- and SO-halo samples, respectively. This confirms that the Peebles spin definition produces results that are quite robust with respect to different halo geometries (see also Fig. 6). The Bullock definition on the other hand is more sensitive to the halo definition and the complicated geometry of FOF-haloes. As a result, it yields systematically different spin distributions for the two halo definitions. Also the median Bullock spin parameter of the FOF-halo sample, $\lambda_{B,FOF} = 0.0414$, is substantially larger than the median value for SO-haloes, $\lambda_{B,SO} = 0.0333$.

The SO-halo result derived with the Bullock spin parameter however resembles the distribution obtained with the Peebles spin parameter in shape, except that the absolute values are systematically shifted to somewhat lower values. In the case of statistically large samples where it is not possible to estimate the concentrations c of every individual halo, the Bullock spin distribution can in fact be simply rescaled by constant factor of 1.1 to yield a spin distribution that almost perfectly reproduces the Peebles spin parameter distribution for a statistically large set of simulated haloes. We explicitly show the shifted Bullock spin parameter distribution in the middle panel of Fig. 4 as red line, which comes to lie just on top of the Peebles spin parameter distribution for SO-haloes. Thus, when comparing mean spin values derived with the two different spin definitions we stress that the constant offset factor of 1.1 has to be taken into account. We want to emphasise that this is true only for SO-haloes, and that the Bullock spin should not be applied to FOF-haloes, as this definition cannot properly take into account the complex geometry of FOF-haloes and results in a spin distribution that is different in shape from the others.

To further depict the differences between the two spin parameter definitions, we compare the Peebles and Bullock spin parameter definitions on a halo-by-halo basis. In Fig. 5 we show the distribution of spins resulting from the Peebles and Bullock spin parameter definitions being applied to the same FOF-haloes (upper panel) or the same SO-haloes (lower panel). Identity is indicated as red line. In the case of FOF-haloes the Bullock spin severely overestimates the spin value for a fraction of the haloes, forming the extended tail in the left upper corner of the upper panel of Fig. 5. Those are haloes significantly extended beyond R_{200} for which the

Bullock spin fails to properly take into account the angular momentum contained in the outer regions of the halo. If SO-haloes are employed, no such systematic bias appears, however, some scatter still remains. Also, the bulk of haloes tends to somewhat higher Peebles than Bullock spin parameters which is another illustration of the constant offset discussed in the middle panel of Fig. 4.

Furthermore, in Fig. 6 we compare the Peebles (upper panel) and Bullock (lower panel) spin parameters derived for the FOF- and SO-counterparts of the same halo. To this end we create a combined halo sample that contains only haloes that match the selection criteria in both the FOF- and the SO-halo definition. Most haloes scatter around the identity line, which is again indicated in red. However, a few percent of the haloes exhibit a significant enhancement in spin in the FOF definition compared to SO. This fraction is somewhat larger for the Bullock spin definition compared to the Peebles definition. The enhancement occurs in aspherical haloes significantly extended beyond R_{200} in their FOF definition (compare to Fig. 1). In the case of the Peebles spin, this enhancement is simply due to additional material, such as from minor mergers at large radii, and affects a smaller number of haloes. On the other hand, when dealing with the Bullock definition this enhancement affects a larger number of haloes and leads to a bias in the resulting mean spin, as this enhancement is not purely of physical nature but partly caused by the fact that FOF-haloes are normalised by virial properties not properly accounting for their true shape. This is also the reason why the Bullock spin parameter distribution of FOF-haloes differs from the SO-halo distribution not only in peak position but also in shape. Thus we want to stress that the Bullock spin parameter appears unsuitable for the FOF-halo definition and should not be applied to intrinsically aspherical FOF-haloes.

To verify our results, we have also applied our group finder and extended halo property calculation to the Millennium Simulation (Springel et al. 2005). From this run we construct an SO-halo sample in the same way we did for *Illustris*, containing $\sim 1.4 \times 10^6$ objects. We plot the resulting Peebles spin parameter distribution as a green line in the lower panel of Fig. 4. It is similar to the distribution we obtain from *Illustris*-1-Dark shown as black line, and exhibits a median value of $\lambda_P = 0.0403$. Note that the imposed 300 dark matter particle cut leads to a higher minimum halo mass in the Millennium Simulation compared to *Illustris* by approximately one order of magnitude. Taking into account the subtle trend of spin with halo mass (compare Fig. 10) the Millennium spin distribution is expected to have somewhat higher values. Furthermore, the Millennium Simulation was carried out with a WMAP1 cosmology, which has a slightly higher σ_8 value than *Illustris*. This makes haloes of a given mass collapse earlier in Millennium than in *Illustris*. Comparing the given distributions is thus the same as making a comparison between spin distributions obtained with the same cosmology but derived at somewhat different times. As shown in the bottom left panel of Fig. 9, the Peebles spin parameter distribution of SO haloes exhibits a small trend to higher values with decreasing redshift, such that the higher σ_8 contributes to the spin distribution derived from the Millennium Simulation being slightly shifted to later times and thus to the right with respect to the one derived from *Illustris*. To avoid such ambiguities and facilitate the comparison

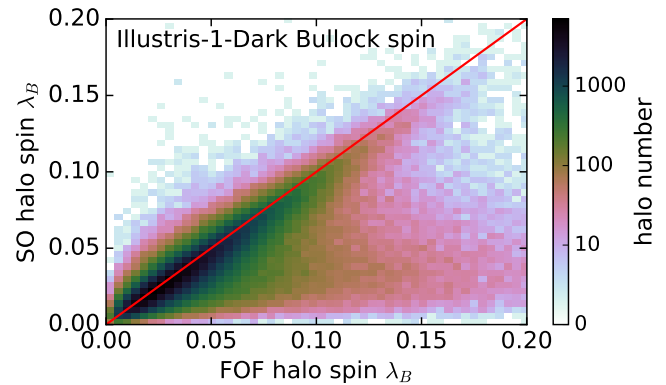
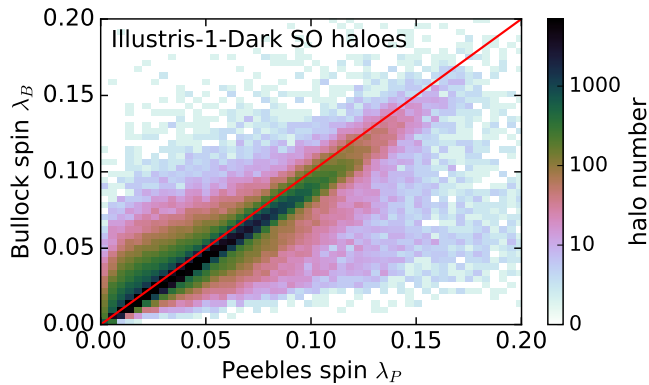
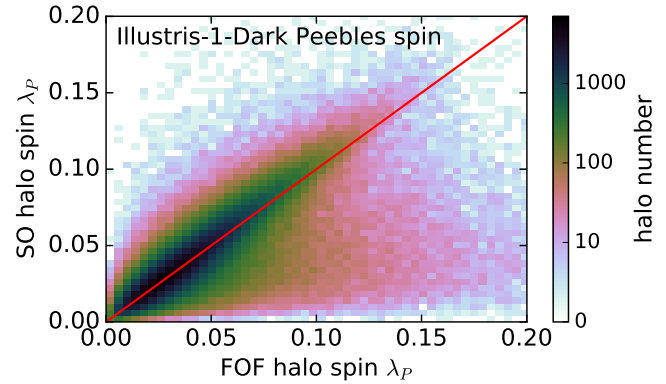
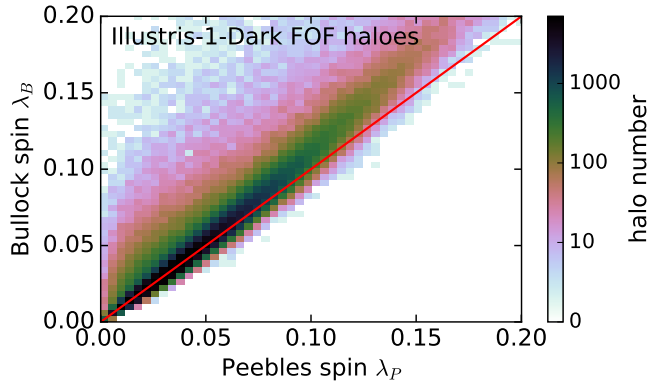


Figure 5. Distribution of the spin parameter values derived with the Peebles and Bullock spin definitions when applied to the same FOF-halo (upper panel) or the same SO-halo (lower panel). The colour scale indicates the number of haloes with certain spin values. Haloes with identical Peebles and Bullock spin parameters would fall onto the red line. We find that for SO-haloes the Bullock spin has to be rescaled by a constant factor of 1.1 to reproduce the Peebles value. In case of FOF-haloes the Bullock definition significantly overestimates the spin for a fraction of haloes as it cannot properly account for the aspherically distributed material at large radii and thus should not be applied to FOF-haloes.

Figure 6. Distribution of the Peebles (upper panel) and Bullock (lower panel) spin parameter obtained by applying the given spin definition to the FOF- and SO-counterparts of the same halo. Most haloes scatter around the red identity line. However, a fraction of the haloes, that is larger in case the Bullock spin is applied, exhibit a significant enhancement in spin for the FOF definition compared to SO. Those haloes are significantly extended beyond R_{200} in their FOF-halo definition (compare to Fig. 1), causing inaccuracies when the Bullock spin definition is used.

between different data sets, we argue in Section 3.3 that it is best to use the Peebles spin parameter of FOF-haloes, as it is the only measure yielding a spin distribution self-similar in time, and as such is least affected by cosmology.

Our Millennium spin distribution can be directly compared to the most precise dark matter only result from the literature, which is given by the best fit from Bett et al. (2007), independently derived for a cleaned halo sample from the Millennium Simulation using the Peebles spin parameter definition and the new fitting function they proposed (red dashed line, see also Section 3.1). The fit to this halo sample is almost identical to their SO-halo sample fit (blue dashed line), and is very close, albeit not identical, to our result. The small residual difference in the spin distribution from Bett et al. (2007) and our study should originate in the details of the selection criteria used to define sets of haloes in quasi-equilibrium. We thus investigate whether sample selection criteria can account for the small differences observed between the spin distributions. We show as red solid line in the lower panel of Fig. 4 the spin parameter distribu-

tion obtained for our SO-halo sample when requiring only a minimum resolution of 300 dark matter particles (identical to Bett et al. 2007) and that haloes have at least one gravitationally bound component. Imposing no limit on the virial ratio allows ongoing mergers to be included in the sample. The angular momentum of haloes in active merging phases has a large and often dominating contribution of orbital angular momentum, leading to an extended tail of the spin parameter distribution to high values. This tail enters the overall normalisation of the spin distribution and lowers its peak value, but the median of the spin distribution is not affected significantly. The changes induced in the spin distribution by different sample selection criteria are thus exactly of the order of magnitude and of the type of the residual differences observed between our results and the study of Bett et al. (2007), validating that our independent analysis methods are consistent.

3 DARK MATTER ONLY RESULTS

3.1 Angular momentum statistics of dark matter haloes at $z = 0$

We begin by presenting the angular momentum properties of dark matter only haloes from Illustris-1-Dark. In Fig. 7 we show the spin parameter distributions for FOF- (upper panel) and SO-haloes (lower panel) at $z = 0$. Our FOF- and SO-halo samples comprise $\sim 400,000$ and $\sim 360,000$ objects, respectively. We provide least-square error fits of the two most common fitting functions to the derived Peebles spin parameter distributions. We chose to present results derived with the Peebles spin parameter, as it yields nearly identical spin distributions for both halo definitions when the potential energy of the halo is estimated accurately. The classic analytic approximation for the spin parameter distribution is the lognormal function (e.g. van den Bosch 1998),

$$P(\log_{10}\lambda) = \frac{1}{\sqrt{2\pi}\sigma} \exp\left[-\frac{1}{2}\left(\frac{\log_{10}(\lambda/\lambda_0)}{\sigma}\right)^2\right], \quad (5)$$

where λ_0 is the peak position and σ the width of the distribution. The lognormal function is normalised such that $\int_{-\infty}^{\infty} P(\log_{10}\lambda) d\log_{10}\lambda = 1$. Bett et al. (2007) performed an extended analysis of the Peebles spin parameter distribution of dark matter only haloes from the Millennium Simulation (Springel et al. 2005) and found that their cleaned halo sample is better described by the fitting function

$$P_B(\log_{10}\lambda) = A \left(\frac{\lambda}{\lambda_0}\right)^3 \exp\left[-\alpha \left(\frac{\lambda}{\lambda_0}\right)^{3/\alpha}\right], \quad (6)$$

where λ_0 is again the peak position, α a free fitting parameter, and A the normalisation, such that $\int_{-\infty}^{\infty} P_B(\log_{10}\lambda) d\log_{10}\lambda = 1$. This new fitting function is constructed to rise with the third power for small values and falls off exponentially for large values. However, this specific shape in combination with the free fitting parameter α makes the given function highly flexible.

We fit both functions to the Peebles spin parameter distributions of our FOF- and SO-halo samples. The small panels in Fig. 7 show the absolute error of the fits relative to the distribution derived from Illustris-1-Dark in every bin. From the absolute errors in every bin we derive the root mean square error ϵ_{rms} of the fit and list it with the best fit parameters in Tab. 2. Based on ϵ_{rms} we find that the new fitting function given by Eq. (6) describes the SO-halo spin distribution slightly better, which is consistent with Bett et al. (2007), who derived their fitting function based on a halo sample very similar to their SO-halo sample. The FOF-halo spin distribution on the other hand is better fit by the classic lognormal function. We find the same behaviour when analysing the Bullock spin parameter distributions. The differences between the two fitting functions lie primarily in the different slopes in the wings of the distribution and the detailed peak shape. However, these differences are relatively small, and which analytic function describes the spin parameter distribution best depends ultimately on the preferred halo definition.

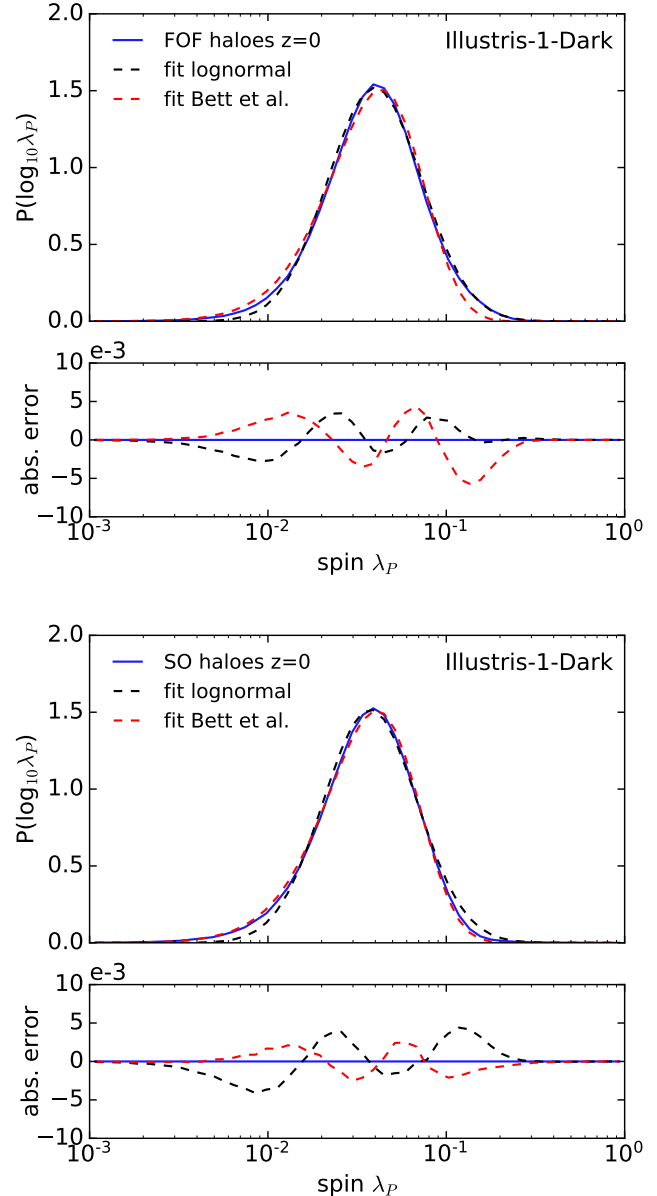


Figure 7. Peebles spin parameter distribution (blue) of FOF-haloes (upper panel) and SO-haloes (lower panel) from Illustris-1-Dark. Both distributions are fitted with a lognormal function (dashed black) and a fitting function proposed by Bett et al. (2007) (dashed red). For easier comparison we show the absolute error of the fitting functions with respect to the distribution obtained from Illustris-1-Dark.

FOF fit lognormal	$\lambda_0 = 0.040$	$\sigma = 0.26$	$\epsilon_{\text{rms}} = 0.0015$
FOF fit Bett et al.	$\lambda_0 = 0.043$	$\alpha = 3.16$	$\epsilon_{\text{rms}} = 0.0022$
SO fit lognormal	$\lambda_0 = 0.037$	$\sigma = 0.26$	$\epsilon_{\text{rms}} = 0.0020$
SO fit Bett et al.	$\lambda_0 = 0.041$	$\alpha = 3.15$	$\epsilon_{\text{rms}} = 0.0011$

Table 2. Best fit parameters of the analytic fits to the Peebles spin parameter distributions derived from Illustris-1-Dark. We give results both for FOF- and SO-haloes, and in each case for the classic log-normal function and the proposed modified fitting function by Bett et al. (2007).

3.2 Convergence

In Fig. 8 we show the Peebles spin parameter distribution for FOF-haloes (upper panel) and SO-haloes (lower panel) derived at three different resolutions of Illustris-Dark (see Tab. 1) for halo masses above $1.4 \times 10^{11} M_{\odot}$. This mass limit is set by our selection criteria, which require a halo to be resolved by at least 300 dark matter particles. When applied to Illustris-3-Dark with the coarsest resolution this corresponds to the above value. As there are subtle trends of spin with halo mass a common mass range must be adopted when examining the numerical convergence of our measurements.

Reassuringly, we find very good convergence of the Peebles spin parameter distribution for the three resolutions of Illustris-Dark. The small residual deviations originate in the limited halo sample size and are consistent with the associated counting noise. The convergence is equally good for the Bullock spin parameter distribution, which we refrain from showing explicitly.

3.3 Redshift evolution of halo spin

In Fig. 9 we show the spin parameter distributions obtained with the Peebles (left column) and Bullock (right column) spin parameter definition for FOF- (upper row) and SO-haloes (lower row) from Illustris-1-Dark for different redshifts. Black dots mark the median spin parameters at every redshift.

The Peebles spin parameter definition applied to FOF-haloes yields a remarkably self-similar spin parameter distribution in time, as expected from theory for self-similar dark matter structures. The self-similarity of haloes is only broken by a varying mean concentration c of the NFW radial density profile with halo mass. Less massive haloes are expected to be on average denser, which corresponds to higher values of c , and to collapse earlier than more massive haloes (Navarro, Frenk & White 1997). This introduces a time dependence of the mean concentration for quasi-relaxed structures thus generally breaking the self-similarity of haloes with respect to both halo mass and time. However, as Navarro, Frenk & White (1997) found no correlation of the spin with concentration (see also Bullock et al. 2001), we expect the spin parameter distribution of haloes to be approximately self-similar with mass and time. This feature is realised by the Peebles spin parameter distribution of FOF-haloes which shows only a small evolution of the median spin value from $\lambda_{z=8} = 0.0374$ at $z = 8$ to $\lambda_{z=0} = 0.0391$ at $z = 0$.

The spin parameter distributions derived with other approaches however exhibit non-vanishing trends with redshift. The strongest shift is visible if the Bullock spin parameter definition is applied to FOF-haloes. The residual trends in this distribution are a consequence of imposing a spherical shape on the more complicated geometry of FOF-haloes. The trends in the distributions obtained from the SO-halo definition are probably caused by not taking into account the gravitationally bound matter outside the virial radius R_{200} , whose relative mass fraction with respect to the matter inside of R_{200} can change over time, inducing the observed trends.

We conclude that although the SO-halo definition is operationally very clean, it is the Peebles spin parameter

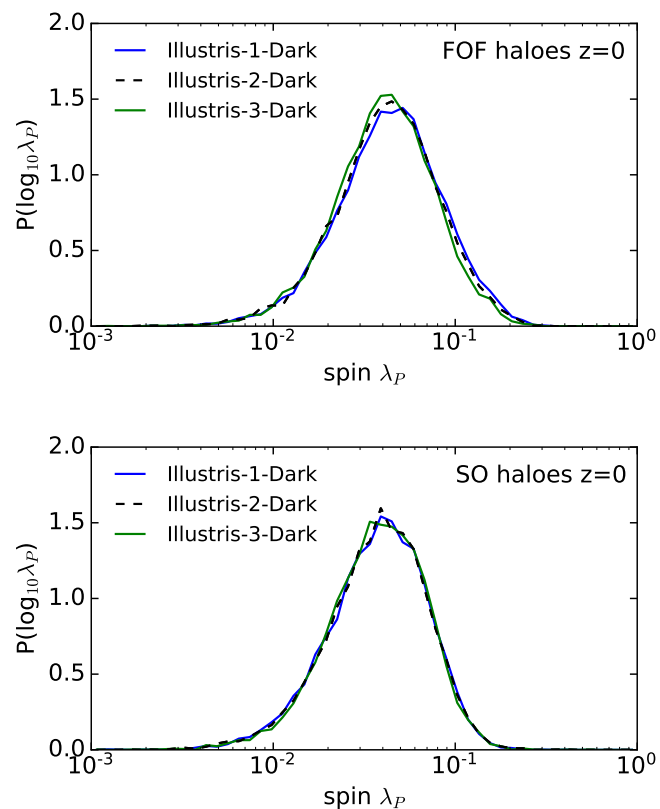


Figure 8. Peebles spin parameter distributions of dark matter only FOF-haloes (upper panel) and SO-haloes (lower panel) derived for the three different resolutions of the *Illustris* simulation suite (see Tab. 1). We find very good convergence for the three resolutions; the small residual deviations are consistent with noise expected from the limited halo sample size.

definition applied to FOF-haloes that yields physically the most stable and reliable results. Thus, in the following we will restrict ourselves to showing mostly results obtained for FOF-haloes with the Peebles spin parameter definition. We have checked that our analysis carried out for SO-haloes yields qualitatively the same results.

3.4 Dependence of spin on halo mass

In Fig. 10 we show the dependence of the Peebles spin parameter of FOF-haloes from Illustris-1-Dark on the halo mass M_{FOF} . This figure shows a two-dimensional histogram where FOF-haloes have been binned according to their mass and spin parameter in 50 equidistant logarithmic bins over the given range. As the absolute number of haloes increases rapidly with decreasing mass, we have normalised every mass bin to unity. The normalised number of FOF-haloes in every mass bin is indicated by the grey shading ranging from a fraction of 0 to 0.2 of the haloes in each mass bin. Contours are drawn at constant fractions of 0, 0.05, 0.1, 0.15, and 0.2, respectively. The median spin parameter in every mass bin is shown as a red line, the overall median spin parameter as a blue line.

Fig. 10 shows a small, but clearly present, systematic increase of the median Peebles spin parameter with halo

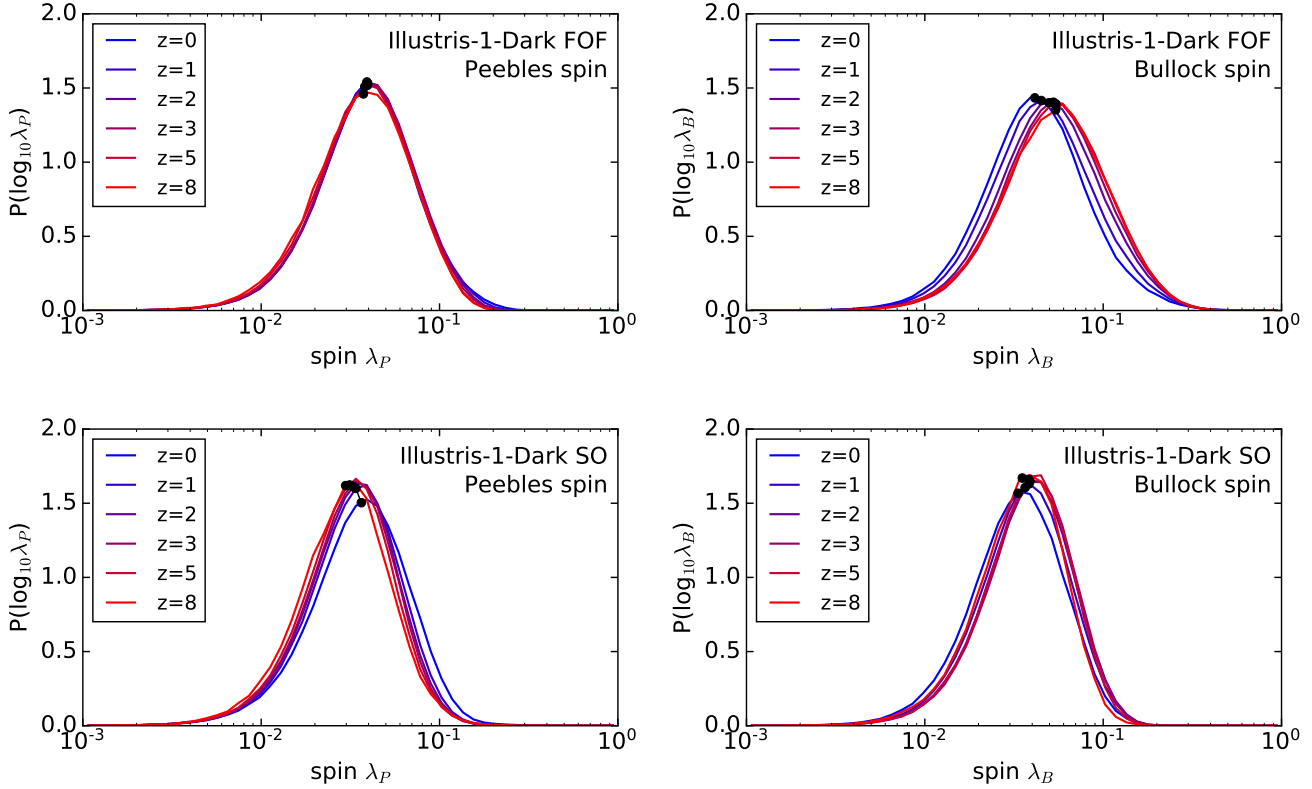


Figure 9. Redshift evolution of the spin parameter distribution of FOF-haloes (upper panel) and SO-haloes (lower panel) derived with the Peebles (left column) and Bullock (right column) spin parameter from Illustris-1-Dark. Black dots mark the median spin parameter at every redshift. The Peebles spin parameter distribution of FOF-haloes is perfectly self-similar with respect to time. The other distributions exhibit residual trends with redshift, which are due to shortcomings in the Bullock spin and SO-halo definitions. We thus restrict ourselves in the following on the Peebles spin applied to FOF-haloes, which yields the most robust results.

mass. This trend is presumably caused by two related effects. More massive haloes originating from larger initial density perturbations are not fully collapsed at $z = 0$ yet. Also, they are still actively accreting matter that perturbs their outskirts and slows down the relaxation process. The orbital angular momentum of the involved minor mergers adds to the intrinsic angular momentum of the main halo and leads to an enhanced spin. As we have shown in Fig. 1, FOF-haloes are in general much more extended than SO-haloes, such that this effect plays a role in FOF-haloes but not in SO-haloes. This is in agreement with the results from Macciò et al. (2007), who find the trend of spin with halo mass to be less distinctive and consistent with zero for SO-haloes.

4 NON-RADIATIVE SIMULATION RESULTS

4.1 Intrinsic differences between dark matter and gas

At high redshift, baryons experience the same gravitational torques from the surrounding density field as dark matter, and thus are assumed to have identical ‘initial’ spins (Fall & Efstathiou 1980). In the absence of any additional physical processes such as star formation and feedback one then naively expects the gas to sustain its initial spin and the correspondence with the dark matter spin.

To test the assumption of gas and dark matter having identical initial spin distributions, van den Bosch et al. (2002) performed non-radiative cosmological simulations that they evolved until a redshift of $z = 3$. Fitting the standard lognormal function to the measured Bullock spin parameter distributions of the dark matter and gas components of their 378 SO-haloes, van den Bosch et al. (2002) derive mean dark matter and gas spin values of $\lambda_{0,\text{dm}} = 0.040$ and $\lambda_{0,\text{gas}} = 0.039$, respectively, confirming that gas and dark matter have identical ‘initial’ spins⁴.

In the upper panel of Fig. 11, we show as solid lines the ‘initial’ dark matter and gas Peebles spin parameter distributions from the non-radiative Illustris-2-NR simulation at $z = 8$ and confirm this result also for the Peebles spin parameter distribution. The derived distributions have median Peebles spin parameters of $\lambda_{\text{dm},z=8} = 0.0335$ and $\lambda_{\text{gas},z=8} = 0.0324$, respectively, which are equal within statistical fluctuations. The dashed lines in Fig. 11 show the same spin parameter distributions at $z = 0$ derived from

⁴ Note that there is no clear definition of ‘initial’ spin to be measured at a distinct cosmic time, as structures acquire their angular momentum continuously by tidal torques from the surrounding large scale gravitational field. However, ‘initial’ spin usually refers to the spin structures have before strong non-linear interactions and galaxy formation physics start playing a significant role.

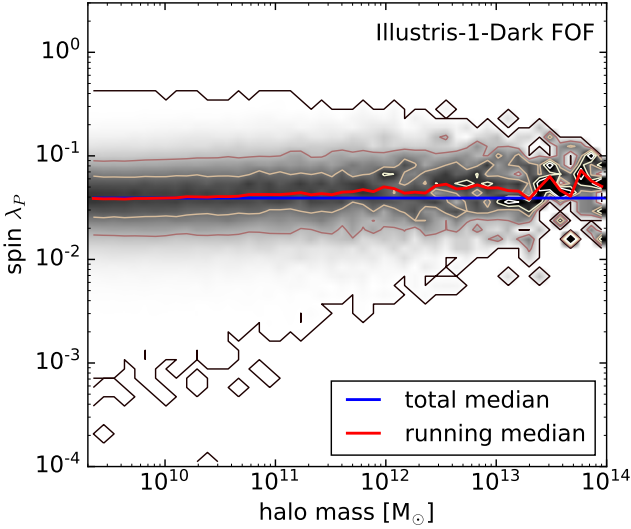


Figure 10. Distribution of the Peebles spin parameter with respect to the mass M_{FOF} of dark matter only FOF-haloes from Illustris-1-Dark, separately normalised in every mass bin. The grey shading ranges from a fraction of 0 to 0.2 of all haloes in a mass bin having a given spin parameter. Contours are drawn at constant fractions of 0, 0.05, 0.1, 0.15, and 0.2, respectively. The total median spin parameter is shown as a blue line, the median of every mass bin as a red line. The median spin parameter slightly increases with increasing halo mass.

$\sim 65,000$ FOF-haloes from Illustris-2-NR. Whereas the spin parameter distribution of the dark matter component exhibits only slightly higher values than the ‘initial’ spin distribution with a median of $\lambda_{\text{dm},z=0} = 0.0377$ at $z = 0$, consistent with the trend in the dark matter only Illustris-1-Dark simulation, the gas component has evolved to substantially higher values with a median spin parameter of $\lambda_{\text{gas},z=0} = 0.0493$. At $z = 0$ this yields a ratio of the median gas to dark matter spin parameter of $\lambda_{\text{gas}}/\lambda_{\text{dm}} = 1.308$, i.e. a $\sim 30\%$ higher spin of the gas than the dark matter.

Similar results have been obtained by Chen, Jing & Yoshikawa (2003) and Sharma & Steinmetz (2005) who performed non-radiative Λ CDM simulations and estimated the mean gas and dark matter spin parameter values from fitting the lognormal to the derived Bullock spin parameter distributions. They arrive at a ratio of mean gas to dark matter spin equal to $\lambda_{0,\text{gas}}/\lambda_{0,\text{dm}} = 1.19$ and $\lambda_{0,\text{gas}}/\lambda_{0,\text{dm}} = 1.44$, respectively, using however much smaller halo sample sizes of 48 and 41 SO-haloes, respectively. The small sample sizes are likely responsible for the variations in the reported size of the effect, but the general trend of having a higher specific angular momentum at $z = 0$ in the gas compared to the dark matter is consistent. Gottlöber & Yepes (2007) quote similar results for more than $10,000$ cluster-sized FOF-haloes with masses larger than $5 \times 10^{13} h^{-1} M_{\odot}$. Applying the same method as above, modulo some uncertainty by applying the Bullock spin parameter definition to FOF-haloes (see Section 2.4), they find a spin parameter enhancement of $\lambda_{0,\text{gas}}/\lambda_{0,\text{dm}} = 1.32$.

Sharma, Steinmetz & Bland-Hawthorn (2012) suggested that the different mechanisms by which dark matter and gas achieve equilibrium lead to an inside-out transport of angular momentum in the dark matter component and

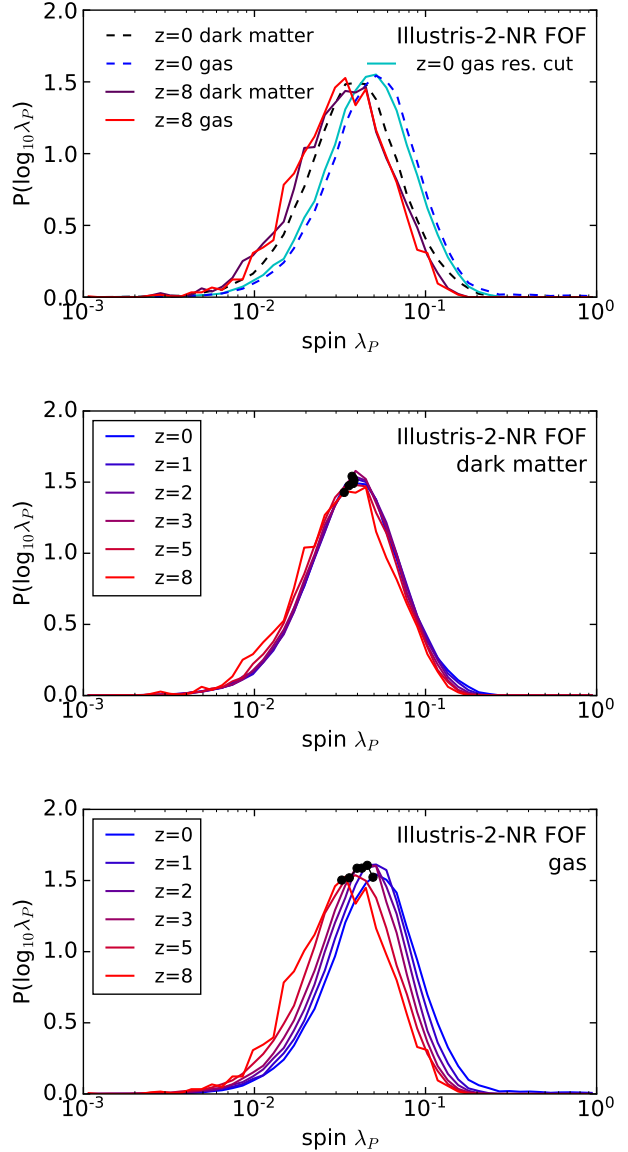


Figure 11. Redshift evolution of the dark matter (middle panel) and gas (lower panel) Peebles spin parameter distributions of FOF-haloes from Illustris-2-NR. Black dots mark the median spin parameter at every redshift. The dark matter spin distribution exhibits the same self-similarity in time as the dark matter-only Illustris-1-Dark simulation, however, at somewhat lower spin values. The spin distribution of gas on the other hand systematically shifts to higher spin values, due to a transfer of angular momentum from dark matter to gas. For comparison, we show (upper panel) the spin parameter distributions for dark matter and gas at $z = 8$ (solid line) and $z = 0$ (dashed line), including the gas distribution derived with a stricter mass cut (cyan) to exclude bias due to poorly resolved haloes.

an outside-in transport in the gas component. The inside-out transport of angular momentum in the dark matter by dynamical friction of mergers entering the inner halo was also already observed by Zavala, Okamoto & Frenk (2008). As the dark matter is insensitive to hydrodynamic interactions, and the total gas mass available for gravitational interactions is small compared to the dark matter mass, the

processes taking place in the two components are largely decoupled from each other. As SO-haloes exclude the outer regions of gravitationally bound haloes (compare Fig. 1), the different transport mechanisms described by Sharma, Steinmetz & Bland-Hawthorn (2012) might explain why the gas to dark matter spin ratio becomes larger than unity for SO-haloes.

When the outer regions are fully included, such as in FOF-haloes, the gas to dark matter spin ratio would be expected to approach unity again in this picture. However, we find an enhanced gas to dark matter spin ratio of the same order of magnitude for FOF-haloes as well, suggesting that different radial redistribution mechanisms of angular momentum in the two components provide an insufficient explanation. Instead, there must be an additional mechanism by which gas acquires more specific angular momentum than dark matter.

In Fig. 11 we show how the Peebles spin parameter distributions of the dark matter (middle panel) and the gas (lower panel) components of FOF-haloes from the Illustris-2-NR simulation evolve with redshift. Black dots mark the median spin parameters at the different redshifts. The dark matter spin parameter distribution exhibits the same self-similarity in time as in the dark matter only Illustris-1-Dark simulation. However, the spin parameter distribution of the gas gradually shifts to higher spin values with decreasing redshift, illustrating a continuous specific angular momentum acquisition in the gas component throughout cosmic time.

This acquisition could be explained by mergers getting ram pressure striped during infall, which leads to a decoupling of their gas and dark matter components. The displacement of the centres of mass of the two components produces a mutual torque of the gas and dark matter components onto each other, allowing a net transfer of angular momentum from the dark matter to the gas. Hydrodynamic shocks and other instabilities occurring in the gas are then crucial for the redistribution of angular momentum inside the gas component, but cannot directly account for transfer of specific angular momentum between dark matter and the gas, as dark matter couples only gravitationally to the gas. The gain of specific angular momentum in the gas is evident in the shift of the gas spin parameter distribution, whereas the corresponding loss of angular momentum in the dark matter distribution is barely visible, as its mass fraction is much larger than that of the gas. Compared to the dark matter spin in the dark matter only Illustris-1-Dark simulation, the gas component gains more specific angular momentum than the dark matter by a factor of 1.26. To compensate for this gain in the gas component, given a cosmic baryon fraction of $f_b = \Omega_b/\Omega_m = 0.1673$, the dark matter component in the non-radiative run has to transfer $\sim 5.2\%$ of its initial spin to the gas. The median dark matter spin parameter in the dark matter only Illustris-1-Dark simulation is $\lambda_{DM} = 0.0391$, which leads to an expected reduced spin parameter of the dark matter component in the non-radiative simulation of $\lambda_{NR,exp} = 0.0371$ at $z = 0$. In Illustris-2-NR we measure a median spin of $\lambda_{NR} = 0.0377$ (also see Fig. 16), but as we observe a weak trend of spin with halo mass (see Section 4.2), we expect such a deviation caused by the different mass cuts in Illustris-1-Dark and Illustris-2-NR.

Furthermore, as we select our haloes based on a mini-

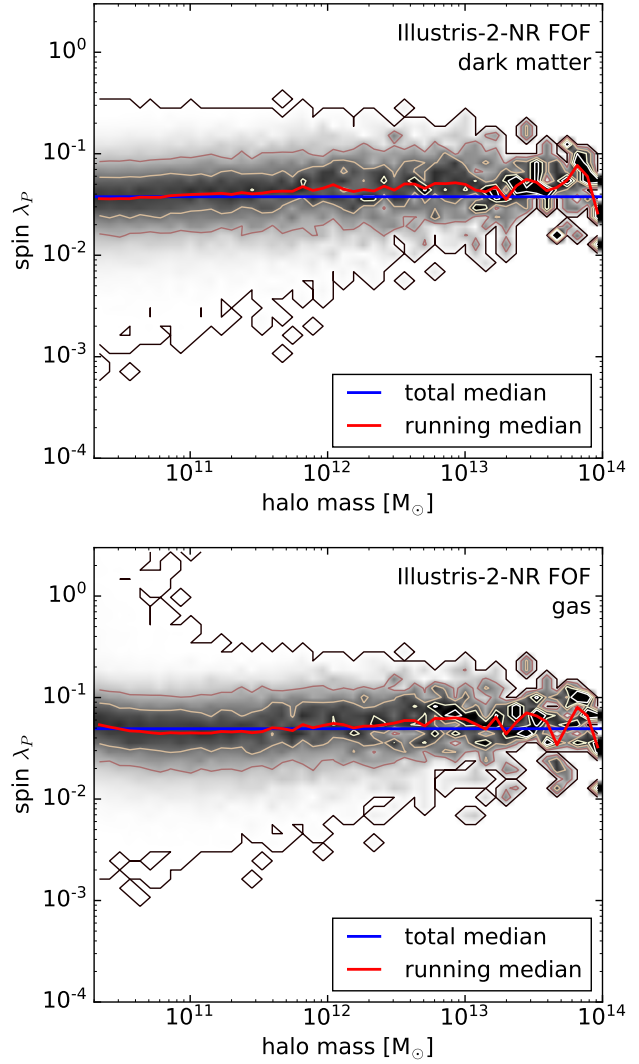


Figure 12. Distribution of the dark matter (upper panel) and gas (lower panel) Peebles spin parameter as a function of FOF-halo mass M_{FOF} for Illustris-2-NR, normalised in every mass bin. The contours are drawn at constant fractions of 0, 0.05, 0.1, 0.15, and 0.2, respectively. The total median spin parameter is shown as blue line, the median of every mass bin as red line. The dark matter spin shows the same trend as in Illustris-1-Dark; the gas spin follows this dark matter trend.

imum number of dark matter particles only, some haloes in our sample have poorly resolved gas components. To quantify the impact from such objects, we show as cyan line in the upper panel of Fig. 11 the gas spin parameter distribution obtained from haloes whose gas component is resolved by at least 300 gas cells. This spin distribution is shifted to slightly smaller spin values compared with the gas distribution from the full sample, but otherwise exhibits the same behaviour. For this restricted sample we find a median value of $\lambda_{gas,z=0}^* = 0.0458$, which corresponds to an enhancement factor of 1.17 with respect to dark matter. The expected dark matter spin in the non-radiative simulation is then $\lambda_{NR,exp}^* = 0.0376$, and thus almost identical to the measured value. However, as poor resolution affects small mass haloes, restricting the sample based on this criterium

introduces an even larger discrepancy in the compared mass ranges, which is a source of bias due to the non-negligible trend of spin with halo mass.

Another possible mechanism that could contribute to the gain of specific angular momentum by the gas component is if there is a preferred orientation of the rotation axis of the gas component perpendicular to the infall directions of merging matter. As we show in Section 5.5, the gas and dark matter component of FOF-haloes are on average misaligned by $\sim 35^\circ$, such that given this preferred orientation the orbital angular momentum of mergers could on average spin up the gas more than the dark matter. Whether such a preferred orientation of the gas component with infalling matter however exists and what may cause it is left for a future investigation.

4.2 Dependence of spin on halo mass

In Fig. 12 we show the dependence of the dark matter (upper panel) and gas (lower panel) Peebles spin parameter of FOF-haloes from Illustris-2-NR on halo mass M_{FOF} . The two-dimensional histogram was obtained in the same way as for Fig. 10. The dark matter exhibits the same trend as already observed in the dark matter only Illustris-1-Dark simulation, with the median Peebles spin parameter increasing slightly with halo mass. The spin parameter of the gas component, though being somewhat higher, follows the same mass trend as observed for the dark matter. The small upward trend in the least massive mass bins is likely due to resolution effects, as the haloes are selected based on being resolved by at least 300 dark matter particles, but there is no limit on the minimum number of gas cells, such that the gas spin parameter of the least massive haloes can be in principle based on only a few dozen cells in gas poor haloes.

5 FULL PHYSICS SIMULATION RESULTS

5.1 Dark matter spin statistics

In this section we present the angular momentum properties of the dark matter component of FOF-haloes from the full physics Illustris-1 simulation and compare them to the dark matter properties derived from the dark matter only Illustris-1-Dark simulation. Illustris-1 comprises $\sim 320,000$ FOF-haloes fulfilling our selection criteria.

In Fig. 13 we show analytic fits of the lognormal and the fitting function proposed by Bett et al. (2007) to the Peebles spin parameter distribution of the dark matter component at $z = 0$. The best fit parameters as well as the root mean square errors of the fits are listed in Tab. 3. These parameters differ only insignificantly from the best fit parameters derived for the Peebles spin parameter distribution of dark matter only FOF-haloes from Illustris-1-Dark that are listed in Tab. 2. Furthermore, we show the convergence of the Peebles spin parameter distribution of the dark matter component for the three different resolutions (see Tab. 1) of the full physics *Illustris* simulations in Fig. 14. We find very good convergence, of the same quality as for Illustris-Dark, with the small deviations originating in the limited halo sample size.

The redshift dependence of the dark matter Peebles spin

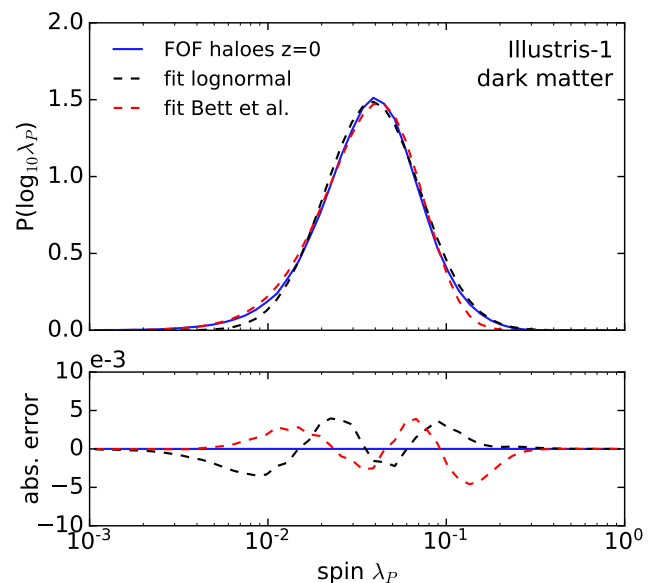


Figure 13. Peebles spin parameter distributions of the dark matter component (blue) of FOF-haloes from Illustris-1 at $z = 0$. The distribution is fitted with a lognormal function (dashed black) and a fitting function proposed by Bett et al. (2007) (dashed red). For better comparison we show the absolute errors of the fitting functions with respect to the distribution obtained from Illustris-1.

fit lognormal	$\lambda_0 = 0.039$	$\sigma = 0.27$	$\epsilon_{\text{rms}} = 0.0018$
fit Bett et al.	$\lambda_0 = 0.042$	$\alpha = 3.30$	$\epsilon_{\text{rms}} = 0.0018$

Table 3. Best fit parameters of the analytic fits to the Peebles spin parameter distributions of the dark matter component derived from Illustris-1. The fit parameters are remarkably similar to the parameters derived for Illustris-1-Dark listed in Tab. 2, showing very good convergence of the dark matter properties.

parameter distribution from Illustris-1 is shown in Fig. 15. Black dots mark the median spin parameter at every redshift. We find the same behaviour of the distribution as in the dark matter only Illustris-1-Dark, in the form of an almost perfect self-similarity in time. A small trend of the median spin towards higher values with decreasing redshift is again present, as already observed in the dark matter spin distributions from both Illustris-1-Dark and Illustris-2-NR.

However, the presence of baryons does introduce subtle changes in the dark matter component, which are barely visible at first sight. To highlight this point, we show in Fig. 16 the dark matter Peebles spin parameter distributions at $z = 0$ derived from the three different simulation types at the highest available resolution (see Tab. 1), the dark matter only simulation Illustris-1-Dark, the non-radiative Illustris-2-NR, and the full physics Illustris-1 simulation. The dark matter Peebles spin parameter distributions derived from these three simulations are remarkably similar. The median spin parameters at $z = 0$ are $\lambda_{\text{DM}} = 0.0391$ for Illustris-1-Dark, $\lambda_{\text{NR}} = 0.0377$ for Illustris-2-NR, and $\lambda = 0.0379$ for Illustris-1. The simulations including baryons thus have slightly smaller median spin parameters than the dark matter only one. The relative shift of the median values amounts to 3.6% for the non-radiative Illustris-2-NR simulation and

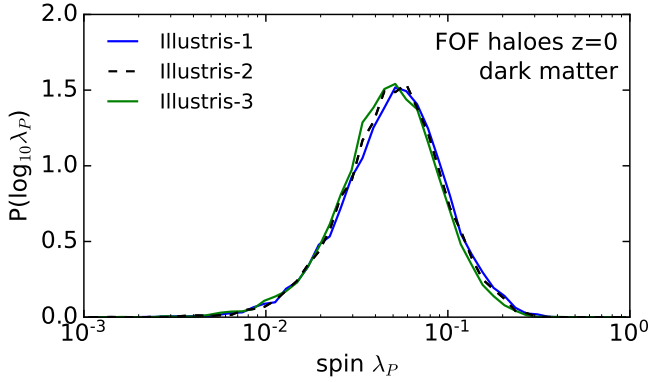


Figure 14. Peebles spin parameter distributions of the dark matter component of FOF-haloes for the three different resolutions of the full physics *Illustris* simulations (see Tab. 1) at $z = 0$. We find good convergence with the small deviations originating in the limited halo sample size.

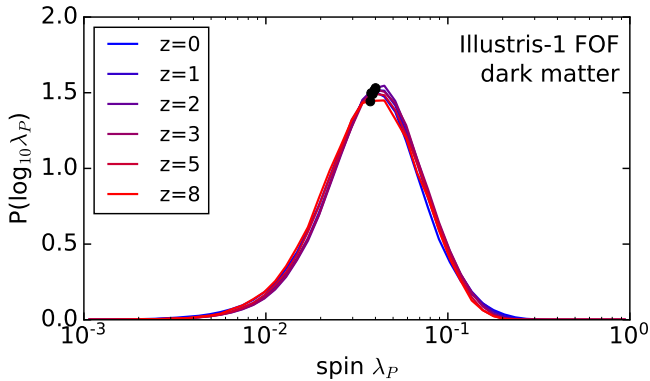


Figure 15. Redshift evolution of the Peebles spin parameter distribution of the dark matter component of FOF-haloes from the full physics *Illustris-1* simulation. Black dots mark the median spin parameter at every redshift. The spin parameter distribution is self-similar in time confirming the dark matter only results.

to 3.1% for the full physics *Illustris-1* simulation compared to the dark matter only *Illustris-1-Dark*. This shift of the dark matter spin distribution to somewhat smaller values in the presence of a baryonic component can be explained as a reflection of the transfer of angular momentum from the dark matter to the gas during mergers, as discussed in Section 4.

5.2 Spin statistics of baryons in different halo regimes

In this section, we investigate the spin statistics of gas and stars within FOF-haloes from *Illustris-1*. The baryonic spin is strongly affected by physical processes such as star formation and feedback, which also indirectly impact the dark matter through the change in baryonic density. These physical processes make the efficiency of galaxy formation a strong function of halo mass, hence we expect the baryonic spin to depend on halo mass as well. This motivates us to

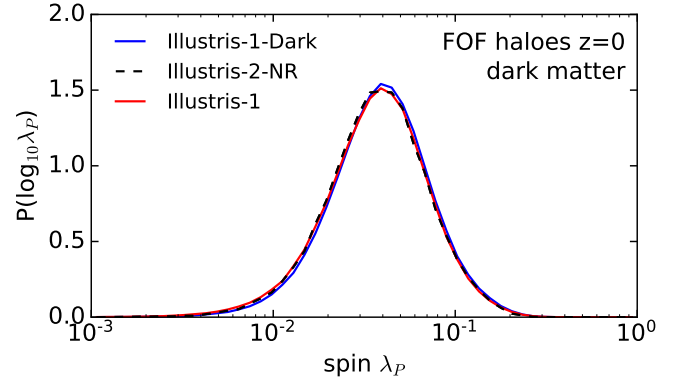


Figure 16. Peebles spin parameter distribution of the dark matter components of FOF-haloes at $z = 0$ from *Illustris-1*, *Illustris-2-NR*, and *Illustris-1-Dark*. The distributions derived from the three different types of simulations are remarkably similar. The median spin parameters are $\lambda_{\text{DM}} = 0.0391$ for *Illustris-1-Dark*, $\lambda_{\text{NR}} = 0.0377$ for *Illustris-2-NR*, and $\lambda = 0.0379$ for *Illustris-1*. Thus the simulations including baryons have a slightly smaller median dark matter spin than in the dark matter only simulation. The relative shift of the median values amounts to 3.6% for *Illustris-2-NR* and 3.1% for *Illustris-1* compared to *Illustris-1-Dark*, consistent with a transfer of angular momentum from dark matter to gas during mergers.

define three mass ranges in which we are going to examine the spin parameter distributions:

- (i) $[2 \times 10^{10} M_{\odot}, 2 \times 10^{11} M_{\odot}]$: SN feedback dominated
- (ii) $[2 \times 10^{11} M_{\odot}, 2 \times 10^{12} M_{\odot}]$: efficiently star forming
- (iii) $[2 \times 10^{12} M_{\odot}, 2 \times 10^{13} M_{\odot}]$: AGN feedback dominated

We discuss the association between these mass bins and the individual feedback regimes further below.

We show the Peebles spin parameter distributions of dark matter, gas, and stars, as well as the combined baryonic and the total spin parameter distributions for *Illustris-1* in the above mass bins in Fig. 17. As the number of haloes increases rapidly with decreasing halo mass (the number of haloes in the three mass bins are 51383, 7286, and 834, respectively), the overall spin statistic is dominated by haloes just above the lower limit of each mass bin. To reduce noise in the highest mass bin, the spin parameter distributions in Fig. 17 have been smoothed with a Gaussian kernel with standard deviation of one bin in spin parameter space and truncated after four bins. The median Peebles spin parameter values in the different mass bins as well as the stellar to gas mass ratios are listed in Tab. 4.

Fig. 17 demonstrates that the scale-dependent galaxy formation physics breaks the self-similarity of haloes with respect to their spin distribution. In realistic simulations of galaxy formation, the gas spin depends strongly on the halo mass (compare also Fig. 19) and is on average about twice as high as the dark matter spin, whereas the stellar spin is only about half as large as the dark matter spin. The general trend of a higher spin of the gas compared with the dark matter, and of a lower stellar spin, is in agreement with findings from Teklu et al. (2015) based on 622 haloes with no restrictions on their dynamical state.

The baryonic spin distribution of low mass haloes (upper panel) is almost completely determined by the gas spin,

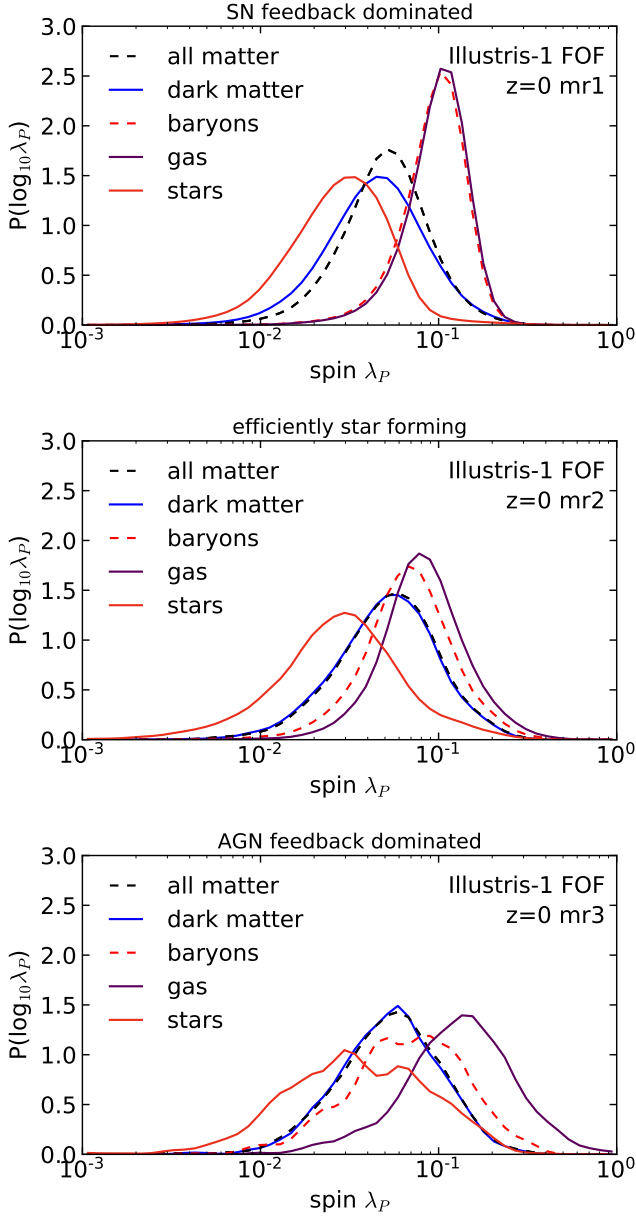


Figure 17. Peebles spin parameter distributions of the dark matter, gas, and stellar component of FOF-haloes as well as the combined baryonic spin parameter distribution and the total spin parameter distribution in the three examined mass ranges of the full physics simulation Illustris-1, as discussed in Section 5.2. This figure demonstrates that galaxy formation physics breaks the self-similarity of the spin parameter distribution observed in dark matter only simulations.

range	all	dm	gas	baryons	stars	$\frac{M_*}{M_{\text{gas}}}$
(i) mr1	0.0506	0.0449	0.102	0.0985	0.0288	0.07
(ii) mr2	0.0534	0.0524	0.0814	0.0681	0.0283	0.38
(iii) mr3	0.0546	0.0541	0.133	0.0692	0.0346	1.61

Table 4. Median Peebles spin parameter values of the different components making up the halo for different halo mass ranges.

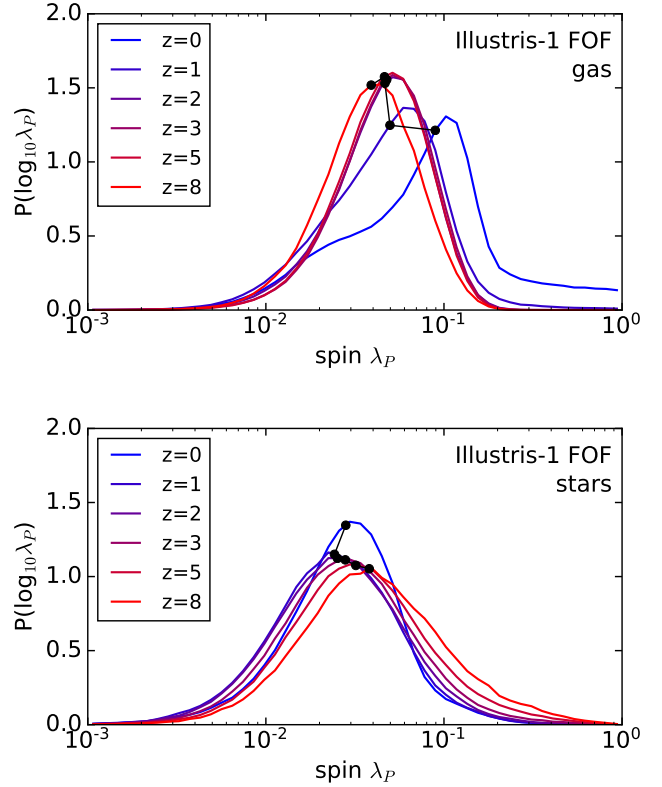


Figure 18. Peebles spin parameter distribution of the gas and stellar component in the full physics Illustris-1 simulation as a function of redshift. Black dots mark the median spin parameter at every redshift. Gas increases its specific angular momentum content with cosmic time. The stellar component on the other hand evolves towards slightly smaller median spins. Both components exhibit changes in the shape of their spin distributions.

as those haloes contain only few stars. With increasing halo mass, the stellar mass to gas mass fraction increases rapidly, and the baryonic distribution shifts to progressively lower spin values (middle and lower panels). The baryonic spin of all haloes from the three mass bins is on average a factor of ~ 1.8 larger than the dark matter spin, which is substantially more than the value of ~ 1.3 found in the non-radiative Illustris-2-NR simulation. We investigate the origin of this enhancement in detail in Section 5.4. The total spin of haloes is thus underestimated by dark matter only simulations by $\sim 13\%$, $\sim 2\%$, and $\sim 1\%$ in the three bins, respectively.

In Fig. 18 we show how the Peebles spin parameter distribution of the gas and stellar component of the full FOF-halo sample from the full physics Illustris-1 simulation evolves as a function of redshift. Black dots mark the median spin parameter at every redshift. The specific angular momentum of the gas component continuously grows with cosmic time. The shape of the gas distribution is getting distorted from the classical lognormal after redshift $z = 2$ due to a second bump emerging at the low tail of the distribution. This low spin bump is caused purely by the smallest mass haloes and vanishes completely if we enforce an additional mass cut on our halo sample at $2 \times 10^{10} M_{\odot}$, equal to the lower bound of the mr1 mass range. This bump could be

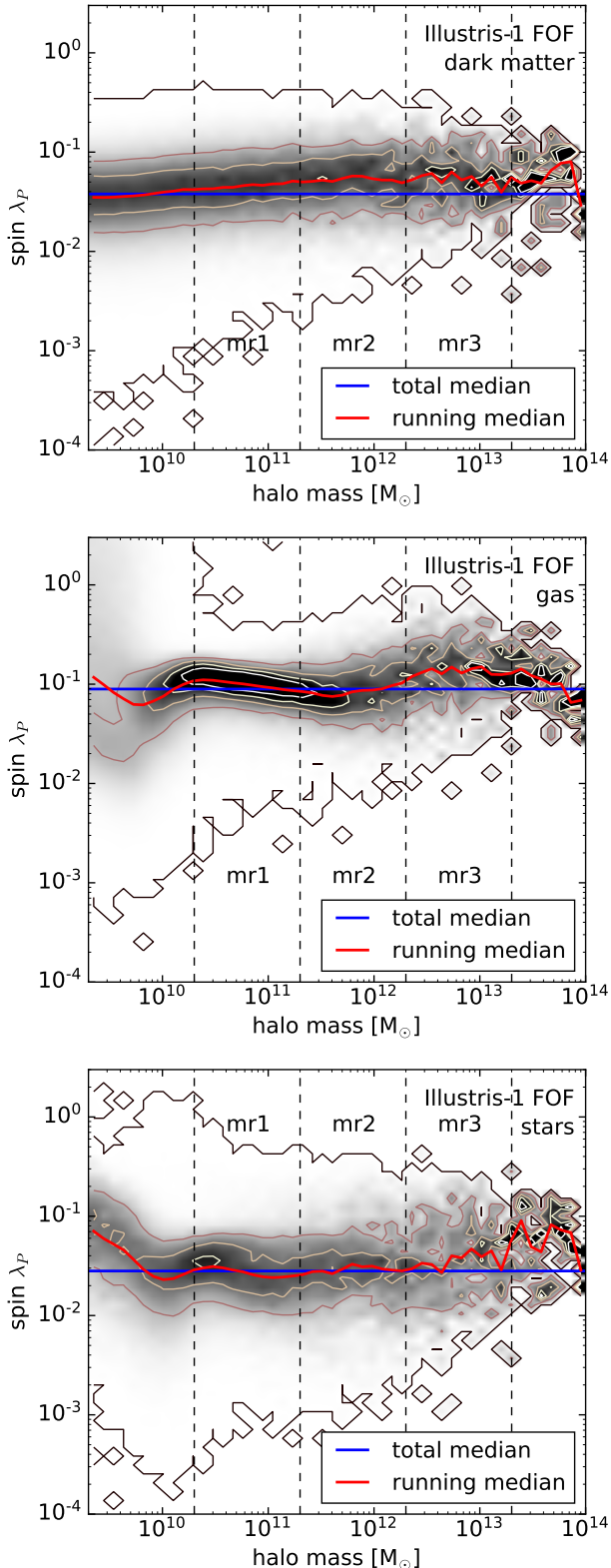


Figure 19. Distribution of the dark matter (upper panel), gas (middle panel), and stellar (lower panel) Peebles spin parameter with halo mass M_{FOF} for Illustris-1 normalised in every mass bin. The grey shading indicates a fraction of 0 to 0.2 of all haloes in a given mass bin having a given spin. Contours are drawn at constant fractions of 0, 0.05, 0.1, 0.15, and 0.2. The total median spin parameter is shown as a blue line, the median of every mass bin as a red line. The dark matter spin shows the same behaviour as in Illustris-1-Dark, the baryonic spin however exhibits a stronger trend with mass that is caused by the impact of feedback. We discuss this trend in more detail in Section 5.2.

explained by the gas component of low mass haloes not gaining any angular momentum due to the lack of mergers and efficient feedback at dwarf halo masses, but also could be purely due to poor resolution of the gas component at these halo masses. The stellar component exhibits a more subtle change in the shape of the spin distribution but evolves to only slightly smaller average spin with cosmic time.

In Fig. 19 we show the detailed mass dependence of the Peebles spin parameter of FOF-haloes from Illustris-1. This figure shows a two-dimensional histogram where FOF-haloes have been binned according to their mass and spin parameter and was obtained as in Figs. 10 and 12 with independently normalised mass bins to account for the variation of halo number with mass. The spin parameter of the dark matter component (upper panel) exhibits the same small increase of the median value with increasing halo mass as observed in the dark matter only Illustris-1-Dark simulation. However, the average spin parameters of the gas (middle panel) and the stellar component (lower panel) show a more pronounced trend with mass, which can be understood as a direct consequence of the impact from feedback.

The two feedback processes perturbing the gas and altering the distribution of baryons are galactic winds driven by supernova (SN) explosions and AGN feedback. SNe occur in cold, dense, star-forming gas regions in the inner halo, which have small specific angular momentum. The wind velocity imparted on the gas by a SN event is taken to be linearly proportional to the one-dimensional velocity dispersion of the halo, as motivated by Okamoto et al. (2010). Details of the prescription can be found in Vogelsberger et al. (2013). For low mass haloes, the winds are more efficient in expelling a fraction of the gas and depleting star formation in the inner regions of the halo. In the *Illustris* simulation, SN feedback plays a major role below a FOF-halo mass of $\sim 2 \times 10^{11} M_{\odot}$. Haloes above this mass are able to retain most of their gas and to actively form stars. Haloes with FOF-halo masses above $\sim 2 \times 10^{12} M_{\odot}$ however grow massive enough black holes such that AGN feedback becomes efficient in quenching their star formation and expelling gas from the halo. As black holes are located in the very centre of haloes, AGN feedback also tends to mostly expel gas with low specific angular momentum from the inner halo.

Considering the halo masses at which the different feedback processes are most efficient, it is easy to interpret the detailed trend of the gas spin with halo mass. Below FOF-halo masses of $\sim 2 \times 10^{11} M_{\odot}$, galactic winds become increasingly effective in expelling low specific angular momentum gas, which leads to an enhanced spin parameter of the remaining gas. Above $\sim 2 \times 10^{12} M_{\odot}$, AGN feedback becomes strong and efficient in expelling the same low specific angular momentum gas. In between these two mass regimes the galaxies are able to hold on to most of their gas and are efficiently star-forming. Correspondingly, they have a lower than average gas spin parameter in this mass bin.

The trend of stellar spin with halo mass arises from the superposition of two effects. Most stars form at around $z \approx 2$, where the gas component is not yet depleted in its content of low specific angular momentum material (compare to Fig. 18). Thus, the bulk of stars forms from the cold, dense gas in the inner halo, which has low specific angular momentum. Furthermore, Zavala et al. (2016) find evidence for old stars to undergo a loss of specific angu-

lar momentum (up to 90%) to the outer dark matter halo through dynamical friction, similar to the loss that occurs in the inner dark matter halo to which old stars are attached. The overall low stellar spin determined by old stellar populations can thus be explained by a combination of both effects. Later on, when low specific angular momentum gas is either locked up in stars or expelled from the inner region due to feedback, star formation extends into the gas reservoir with higher specific angular momentum that now refills the inner halo. Thus young stars have an enhanced spin on average, tracking the higher spin parameter of the still available gas (see also Teklu et al. 2015; Zavala et al. 2016). This imprints a trend of spin with halo mass similar to the one exhibited by the gas spin on top of the otherwise constant low stellar spin.

As pointed out by Zavala, Okamoto & Frenk (2008), and more recently by Zavala et al. (2016) this behaviour is also closely related to the morphology of the galaxy forming at the halo centre. Those authors have shown that if most star formation takes place before turnaround, the stars are attached to dark matter clumps forming the inner halo and likewise lose a significant fraction of their specific angular momentum to the outer halo, leading to the formation of an elliptical galaxy. On the other hand, when star formation in the inner region is suppressed before turnaround, high specific angular momentum gas can penetrate the inner halo region at later times and form a stellar disc. Thus the precise strength and timing of the feedback events that determines the amount of expelled gas from the inner region and whether it overcomes the gravitational potential of the halo is crucial for the morphology of the central galaxy. In *Illustris* we find a morphological mix of galaxies that is consistent with observations, which makes this simulation particularly suitable for the investigation of the impact of feedback onto the angular momentum properties. Rodriguez-Gomez et al. (2016) further investigate the connection between galaxy morphology, halo spin, and merger history. In future studies it will be crucial to disentangle the feedback induced mechanisms leading to the redistribution of matter and specific angular momentum inside of haloes and to quantify the impact on galaxy morphology.

We refrain from a detailed interpretation of the results at the very high mass end of the distribution as it is affected by small number statistics. Also, we disregard trends below a mass of $10^{10}M_{\odot}$ as our haloes were selected based on a minimum dark matter particle number and thus the gas and stellar spin parameters below this mass scale can be affected by resolution effects.

5.3 Specific angular momentum distributions of dark matter and gas

In order to understand whether galactic winds and AGN feedback can on average expel a sufficient amount of low angular momentum gas from the halo to account for the apparent gain of specific angular momentum in the baryonic component we observe, we need to turn to the distribution of specific angular momentum *inside* a halo. This has so far been extensively studied for dark matter only haloes but not for the baryonic component. Bullock et al. (2001) suggested a universal angular momentum profile for the distribution

of specific angular momentum inside a halo given by

$$M(< j_{\text{sp}}) = M_{\text{tot}} \frac{\mu j_{\text{sp}}}{j_0 + j_{\text{sp}}}, \quad (7)$$

where j_{sp} is the specific angular momentum of dark matter projected onto the rotation axis of the whole halo, $M(< j_{\text{sp}})$ the cumulative dark matter mass of the dark matter with specific angular momentum smaller than a given value j_{sp} , and M_{tot} denotes the total halo mass. μ and j_0 are two fitting parameters that are not mutually independent. Bullock et al. (2001) derived the universal angular momentum profile from dark matter only SO-haloes, such that $M_{\text{tot}} = M_{200}$.

Above we deliberately used the term ‘dark matter’ instead of ‘dark matter particle’, as the specific angular momentum distribution is here meant to apply to the mean streaming velocity of the material, not to individual particles. Due to the finite velocity dispersion of the dark matter, a substantial fraction of the dark matter particles can actually be counter-rotating with respect to the net rotation direction. To account for this effect one needs to average over a sufficiently large number of dark matter particles to obtain a fair estimate of the mean streaming velocity and the specific angular momentum. To derive specific angular momentum distributions we thus bin the dark matter particles in spherical shells around the halo centre of 1000 particles each, and use the specific angular momenta and masses of the spherical bins as data points for the distribution.

Because searching the whole simulation volume for particles and cells belonging to every SO-halo is computationally expensive in post-processing, we simplify the present analysis by applying the R_{200} cut only to particles and cells belonging to the corresponding FOF-halo. As we here analyse only very massive and extended haloes, the number of particles/cells being part of the SO-halo but not part of the corresponding FOF-halo is negligible. However, we caution that this is not generally true, especially for low mass haloes. We also want to remark that deriving specific angular momentum distributions for FOF-haloes can be more problematic, as in the outskirts a significant fraction of the angular momentum is carried by the orbital angular momentum of minor mergers, which can have infall trajectories counter-rotating with respect to the main halo. Simply removing the resulting bins with negative specific angular momentum introduces a discrepancy in the total halo mass, such that we refrain from adopting this approach.

In Fig. 20 we show the specific angular momentum distributions derived for the different halo components of a randomly selected massive halo from *Illustris-1* at $z = 0$ and $z = 5$. We fit the universal angular momentum profiles given by Eq. (7) to the dark matter, gas, and stellar specific angular momentum distributions. To this end we bin the data points in 60 equidistant bins in the full j_{sp} -range and provide least square error fits to the average values in those bins. We ignore the 10 lowest bins, as those contain only few or no data points at all, leaving 50 values for determining the best fit. Note that μ and j_0 are not independent fitting parameters. Defining $m = M(< j_{\text{sp}})/M_{\text{tot}}$ one can rewrite Eq. (7) as

$$j_{\text{sp}}(m) = \frac{mj_0}{\mu - m}, \quad (8)$$

such that the universal angular momentum profile can be

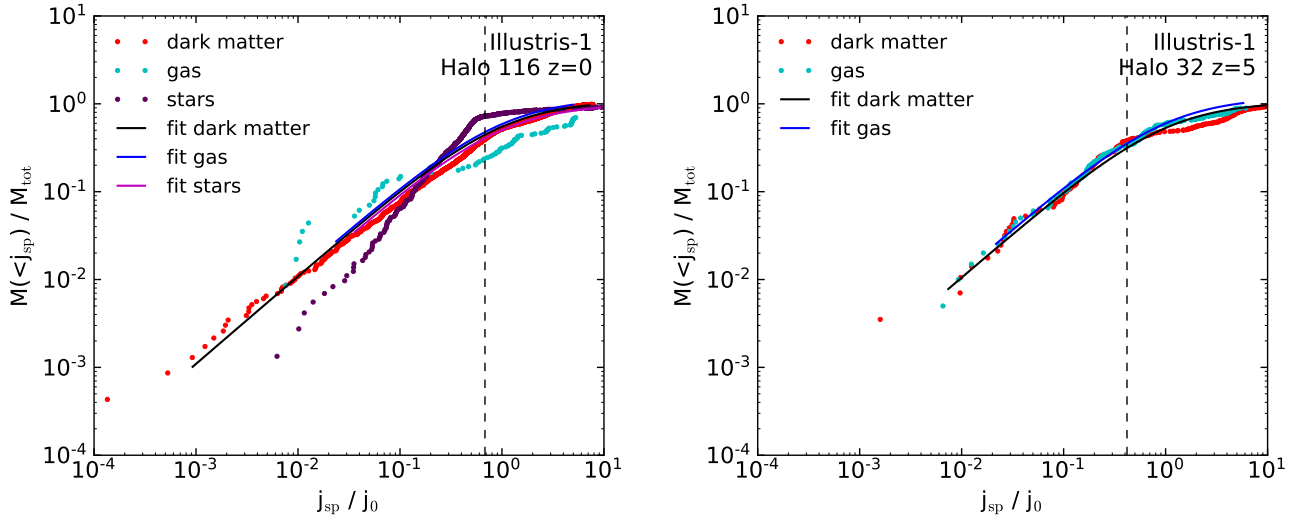


Figure 20. Specific angular momentum distributions of a random halo from Illustris-1 at $z = 0$ and $z = 5$, obtained by binning the dark matter, gas, and stars in spherical bins of 1000 dark matter/star particles or gas cells each and calculating the specific angular momentum in each bin. The bins are then sorted by their specific angular momentum value projected onto the normalised total angular momentum of the whole halo. The distributions show the cumulative mass $M(< j_{\text{sp}})$ of all bins with j_{sp} smaller than a given value. Solid lines show least square error fits of the universal angular momentum profile to the derived distribution approximated by 50 mean values estimated in equidistant logarithmic bins. At high redshift, the universal profile is a good fit to both the dark matter and gas distributions. However, at $z = 0$, this is true only for dark matter, indicating that the gas distribution gets highly perturbed by feedback processes during the subsequent evolution, causing also the stellar distribution to be perturbed away from the universal profile. The black dashed line marks the average j_{sp} value below which the gas is expelled from the halo due to feedback. See Section 5.4 for more details.

reduced to a one parameter function where the two fitting parameters μ and j_0 are related by

$$j_{\text{sp}}^{\text{tot}} = j_0 \int_0^1 \frac{m}{\mu - m} dm = j_0 [-\mu \ln(1 - 1/\mu) - 1]. \quad (9)$$

Here $j_{\text{sp}}^{\text{tot}}$ is the absolute value of the total specific angular momentum of the halo subset considered, and $\mu > 1$.

Fig. 20 shows that at high redshifts the dark matter and gas components of a halo have identical ‘initial’ specific angular momentum distributions and as such also spin parameters. This is a direct consequence of the ‘initial’ spin of dark matter and gas being caused by large scale tidal torques from the surrounding gravitational field, which acts the same way on all matter species. The universal angular momentum profile, derived for haloes at $z = 0$, turns out to be a reasonably good approximation of the specific angular momentum distribution at high redshift, in agreement with dark matter mostly sustaining its ‘initial’ spin.

Consistently, the universal angular momentum profile is a good fit to the dark matter specific angular momentum distribution at $z = 0$. The gas component at $z = 0$ is however significantly perturbed by the action of feedback which sets in at later times such that the gas distribution does not follow the universal profile any more. This also causes the angular momentum distribution of stars to deviate from the universal profile. Furthermore, the gas distribution lacks the low specific angular momentum part of the gas that is still present in the dark matter, as it was either locked up in stars or expelled by feedback. Though the best fit universal angular momentum profiles are identical for all halo components, the true distributions of the specific angular

momentum of gas and stars inside a halo exhibit very different features than prescribed by the universal profile. We have investigated the gas specific angular momentum distributions of many haloes and find a large variety in their distributions with little commonality, thus not lending itself to a description through a simple universal function. Instead, the specific angular momentum distribution of gas inside a halo depends strongly on the particular history of the individual halo.

5.4 The origin of the baryonic spin enhancement

In Section 5.2 we have shown that the baryonic component of haloes shows an enhanced spin compared to the dark matter. Taking the average of all haloes contained in the three examined mass ranges we find a baryon to dark matter spin parameter ratio of ~ 1.8 . We can use the universal angular momentum profile from Bullock et al. (2001) to estimate the expected enhancement of the baryonic spin parameter when a fraction of the low specific angular momentum gas is expelled from the halo due to feedback, allowing us to investigate whether this already explains the observed enhancement. To this end, we however need to know how much baryonic mass is on average still present in a halo at $z = 0$.

In a quiet environment with no feedback at work the baryon to total mass ratio of haloes should equal the universal cosmic baryon fraction, $f_b = \Omega_b/\Omega_m = 0.1673$. With feedback physics at work we find an average baryon to total mass fraction of SO-haloes from Illustris-1 at $z = 0$ of $f_{\text{halo}} = M_{\text{baryons}}/(M_{\text{dm}} + M_{\text{baryons}}) = 0.0963$, which is significantly below the cosmic baryon fraction. Compared to

the cosmic average, SO-haloes thus lose on average $f = (f_b - f_{\text{halo}})/f_b \approx 42\%$ of their initial gas mass.⁵ This is in very good agreement with Sharma, Steinmetz & Bland-Hawthorn (2012) who find an excess of low angular momentum gas in their non-radiative simulations that yields an angular momentum distribution incompatible with the exponential density profile of spiral galaxies. Those authors show that this discrepancy cannot be alleviated by different merger histories and the redistribution of angular momentum associated with those, and estimate that haloes have to lose $\sim 40\%$ of their low angular momentum gas for most of their haloes to host disc galaxies.

As feedback occurs in star-forming regions that are comprised of cold, dense, and slowly rotating gas, it expels gas with low specific angular momentum. The high specific angular momentum is then redistributed within the remaining gas creating a new tail of low specific angular momentum gas. This new tail is due to gas that is now entering the inner halo, and will typically be less prominent than before the onset of feedback. In our calculation we therefore assume that it is always the gas with the lowest specific angular momentum that is expelled from the halo. With this ansatz and making use of the fact that gas (and thus baryons, as there are only few stars at high redshift) and dark matter have identical ‘initial’ universal angular momentum profiles, we can calculate the specific angular momentum of the remaining baryons $j_{\text{sp},f}$ by integrating the universal angular momentum profile over the remaining mass, which simply corresponds to integration limits from $f = 0.42$ to 1,

$$\begin{aligned} j_{\text{sp},f} &= \frac{j_0}{(1-f)} \int_f^1 \frac{m}{\mu - m} dm \\ &= \frac{j_0}{(1-f)} \left[-\mu \ln\left(\frac{\mu-1}{\mu-f}\right) - (1-f) \right]. \end{aligned} \quad (10)$$

The factor $1/(1-f)$ is introduced to account for the fact that the specific angular momentum $j_{\text{sp},f} = J_f/(1-f)M_{\text{tot}}$ is now obtained from the remaining baryons which have a reduced mass of $(1-f)M_{\text{tot}}$ compared to the initial mass of the baryonic component. In Fig. 20 we indicate the lower integration limit f as black dashed line.

Bullock et al. (2001) found that 90% of their haloes lie in a parameter range of $\mu \in [1.06, 2]$. Inserting these two limiting values⁶ in Eq. (9) and Eq. (10), and taking the ratio of these two equations, we arrive at an enhancement of the specific angular momentum of the baryonic component by

$$\frac{j_{\text{sp},f}}{j_{\text{sp}}} [\mu = 1.06 - 2] = 1.63 - 1.49. \quad (11)$$

Thus we find a relative boost in the spin parameter of the baryonic component of ~ 1.55 due to expulsion of low specific angular momentum gas from the halo by feedback.

⁵ For FOF-haloes we obtain $f \approx 48\%$ which in the end yields very similar results. However, we carry out our calculation for SO-haloes, because the universal angular momentum profile was shown to hold for this type of halo.

⁶ We adopt the values given by Bullock et al. (2001), as those were derived from a statistical sample of ~ 200 haloes with > 6000 resolution elements, and verified on ~ 400 haloes with > 1000 resolution elements. We have analysed the angular momentum distributions only for ~ 20 individual haloes, but find shape parameters consistent with the given range.

Combined with the ‘inherent’ increase in gas spin discussed in Section 4 by a factor of ~ 1.3 due to a transfer of specific angular momentum from the dark matter to gas, this yields an overall enhancement by a factor of ~ 2 relative to the dark matter spin. This value is somewhat overestimated as it does not take into account that some of the low specific angular momentum gas is locked up in stars or otherwise remains in the halo and contributes to the average baryonic spin at $z = 0$. However, our estimate also assumes instantaneous removal of low angular momentum gas, whereas in reality feedback is a continuous process taking place at the inner halo which is constantly refilled with relatively low angular momentum gas. An analysis invoking tracer particles following the gas flow and recording its history in detail will be crucial to accurately pin down the fraction of low angular momentum gas still remaining in the halo. In this study, we merely provide an estimate of an upper limit for the enhancement of baryonic spin based on the assumption that feedback instantaneously expels gas with the lowest specific angular momentum. In that sense, the observed enhancement of the spin of the baryonic component of ~ 1.8 can be solely explained by the combined effects of the removal of low specific angular momentum gas from haloes by feedback and the ‘inherent’ spin enhancement of the gas component due to angular momentum transfer from dark matter to the gas during halo assembly, which is already captured in non-radiative simulations. As our analysis is based on more than 320 000 haloes, this shows that (in a statistical sense) it is not necessary to invoke cold filamentary gas accretion as an additional source for the enhanced baryonic spin. The enhancement of baryonic spin due to cold flows was discussed in detail by Danovich et al. (2015) using 29 individually selected Milky Way sized galaxies at redshifts $z = 4 - 1.5$ from a cosmological simulation carried out with ART. Further support for this mechanism was recently provided by Stewart et al. (2016) based on simulations of a single Milky Way sized galaxy with multiple hydrodynamic codes, strengthening cold filamentary accretion as a code-independent viable mechanism for baryonic angular momentum gain in individual objects. However, Sales et al. (2012) showed that filamentary gas accretion from misaligned filaments can also lead to the opposite behaviour, a reduced spin of the baryonic component and the formation of an elliptical galaxy in the halo centre. The statistical relevance of cold flows as a source for baryonic spin enhancement thus still has to be established in future studies. Our results suggest that this mode may be relevant only in selected objects.

5.5 Misalignment between the halo components

Finally, we want to briefly analyse the distributions of misalignment angles between the angular momentum vectors of the different halo components and how they evolve with redshift. We quantify the misalignment by the cosine of the misalignment angle between two halo components,

$$\cos(\vartheta) = \frac{\mathbf{J}_1 \cdot \mathbf{J}_2}{J_1 \cdot J_2}, \quad (12)$$

where $\mathbf{J}_{1/2}$ are the angular momentum vectors of two different halo components, such as dark matter, gas, or stars and $J_{1/2} = |\mathbf{J}_{1/2}|$ their absolute values. In Fig. 21 we show the distribution $P(\cos(\vartheta))$ of misalignments as a function of

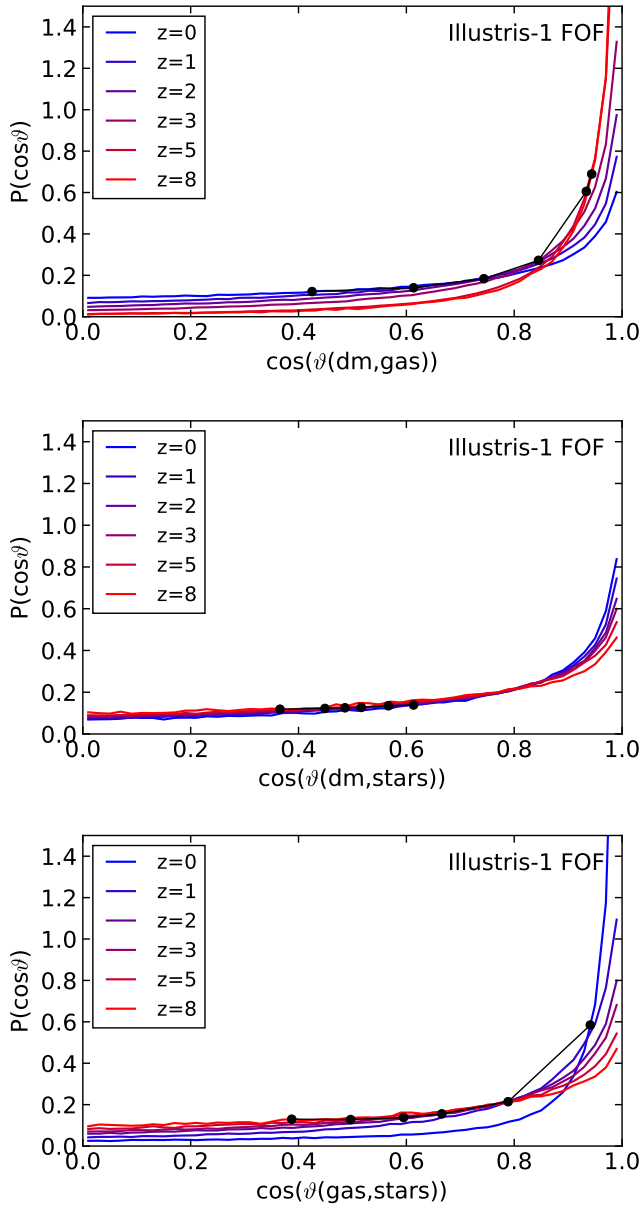


Figure 21. Redshift evolution of the distribution of misalignment angles between the different halo components for FOF-halos from Illustris-1. During cosmic evolution the dark matter and the stellar component (middle panel) as well as the gas and the stellar component (lower panel) become more aligned, whereas the misalignment between the dark matter and gas (upper panel) grows with cosmic time.

redshift. Black dots mark the median misalignment at every redshift. The distributions were derived by binning all FOF-halos from Illustris-1 in 50 equidistant bins, covering the range of misalignments between $\cos(0^\circ) = 1$ (perfectly aligned) and $\cos(90^\circ) = 0$ (perpendicular), and normalising to the total number of haloes as well as the bin size. We refrain from showing the distributions up to $\cos(180^\circ) = -1$ (anti-aligned), as in this range the distributions are a continuous extrapolation of the trend visible in the presented range. We caution that the halo samples are always dominated by the lowest mass haloes whose gas and stellar com-

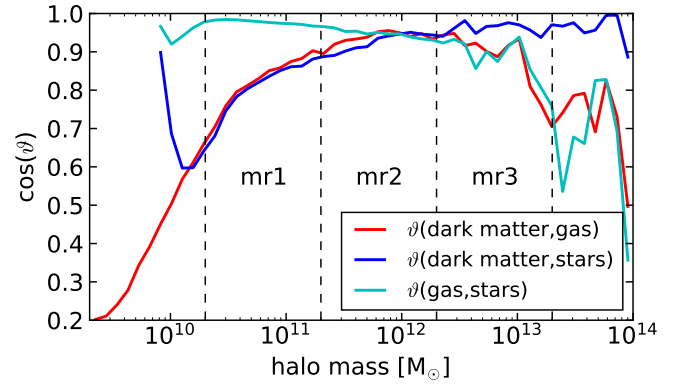


Figure 22. Median misalignment between the different FOF-halo components from Illustris-1 as a function of halo mass. Best alignment between all halo components can be found in Milky Way sized haloes where the impact from feedback is weak. In general, the alignment of halo components is a strong function of halo mass, for a detailed discussion see Section 5.5.

ponents can be affected by poor resolution. However, we refrain from imposing an additional mass cut on our halo samples, because this would remove most of the haloes at high redshift.

We find that the dark matter and the stellar component (middle panel), as well as the gas and the stellar component (lower panel) become progressively more aligned towards lower redshift, whereas the misalignment between the dark matter and gas (upper panel) grows with cosmic time. The growing misalignment between the gas and dark matter component is a natural consequence of the feedback mechanisms continuously perturbing the gas but having only indirect and weak effects on the dark matter through the change of the baryonic density distribution.

In Fig. 22 we show the median misalignment as a function of halo mass and thus feedback regime at $z = 0$, derived by binning the FOF-halos from Illustris-1 in 50 equidistant logarithmic bins in the given mass range and calculating the median misalignment $\cos(\vartheta)$ in every bin. The vertical dashed lines single out the three mass ranges introduced in Section 5.2. Below a FOF-halo mass of $\sim 10^{10} M_\odot$ the median misalignment between stars and both the dark matter and gas exhibits a steep upward trend that is due to poor resolution of the stellar component. Above $\sim 2 \times 10^{13} M_\odot$ our results are affected by small number statistics. Within the singled out intermediate mass ranges we find best alignments of all three components in Milky Way sized haloes where the impact from feedback is weak (see Section 5.2). The alignment between dark matter and gas becomes worse in less and more massive haloes, as at those halo masses the gas component is perturbed by galactic winds and AGN feedback, respectively. The median misalignment angle across all three mass ranges is $\vartheta(\text{dm, gas}) = 34.2^\circ$. Stars are almost perfectly aligned with the gas at small halo masses and exhibit the same misalignment with dark matter as the gas component. With increasing halo mass the stellar component becomes progressively better aligned with dark matter and correspondingly less well aligned with the gas. Within the three mass ranges we find median misalignment angles of $\vartheta(\text{dm, stars}) = 35.7^\circ$ and $\vartheta(\text{gas, stars}) = 12.1^\circ$.

This trend can be possibly explained by massive haloes hosting elliptical galaxies comprised of mostly old stars, which are subject to gravitational interaction with dark matter but are not affected by the hydrodynamical interaction that the gas undergoes during the phase of late-time halo assembly. The stellar populations in low mass haloes will be typically younger and thus are expected to exhibit an angular momentum vector oriented along the rotational direction of the gas out of which these stars were formed.

Our results seem generally consistent with previous studies, however a direct comparison is often difficult due to the variety of adopted approaches in the literature, such as measuring the misalignment for specific galaxy types, or only in the inner region of haloes. We leave a detailed investigation of feedback induced misalignments between different halo components, as well as a study of radial trends in the spin alignment to future studies.

6 DISCUSSION AND CONCLUSIONS

In this work, we have analysed the distribution of halo spins in the *Illustris* simulation suite, one of the first simulations of galaxy formation with full hydrodynamics that produces a realistic galaxy population in a sizeable volume, thus also yielding good statistics, comparable to the best dark matter only simulations that have been used for the study of these properties in the past. Our goal has been a characterisation of the global angular momentum content of haloes as a function of mass and time in this new generation of hydrodynamical simulations, and to highlight the differences with respect to dark matter only results.

To shed some light on the different approaches adopted in the literature for measuring halo spin statistics, we have analysed the systematic differences between the commonly used Peebles and Bullock spin parameter definitions, and between the friends-of-friends (FOF) and spherical overdensity (SO) halo definitions. Also, we have checked the impact of sample selection criteria designed to single out structures in quasi-equilibrium. For this investigation we have employed a large sample of $\sim 400,000$ dark matter only FOF- and $\sim 360,000$ SO-haloes from *Illustris-1-Dark*. The Peebles definition yields robust spin parameter values for both halo definitions, an advantage over the simpler Bullock parameter which has problems to cope with the extended geometry of FOF-haloes. We find that for SO-haloes the Bullock spin parameter needs to be rescaled by a constant factor of 1.1 to yield the same mean value as the Peebles parameter, when the concentration dependence is ignored. When comparing spin parameters derived with the different definitions it is thus necessary to bear this offset in mind. Finally, we find that sample selection criteria have a small effect on the resulting spin parameter distributions. The differences are of the same order of magnitude as the variations between different results presented in the literature, and thus can explain those discrepancies.

Interestingly, we find that only the Peebles spin parameter definition applied to FOF-haloes yields a spin parameter distribution that is self-similar in time to high accuracy. It is thus worthwhile to make the extra effort of accurately calculating the gravitational binding energy of haloes and use the Peebles definition to characterise the angular momentum

content of haloes. For this purpose, we use the tree-gravity solver of AREPO for all haloes (as well as all subhaloes, but these are not studied here) of the *Illustris* simulation suite and include the corresponding results in a group catalogue extension. Our augmented group catalogue furthermore contains the kinetic energies of FOF- and SO-haloes (and subhaloes) as well as the angular momentum vectors of the dark matter, gas, and stellar component of these. A full list of all properties available in the group catalogue extension can be found in the Appendix, and these data will be added to the public data release of *Illustris* (Nelson et al. 2015).

With respect to the dark matter, we reproduce the well known result of finding essentially no mass- and redshift dependence of the spin parameter distribution. However, the subtle trend of spin with halo mass and the fact that the number of haloes steeply increases with decreasing halo mass causes the average spin of a halo sample to be always dominated by the smaller haloes with lower spin and thus the resolution limit of the simulation. This has to be borne in mind when comparing literature results.

When baryons are added, the dark matter component retains its properties. The baryons, however, exhibit a substantial gain in specific angular momentum that increases towards low redshift. Already in the non-radiative case, where one may naively expect both dark matter and gas to retain their identical initial spins, we find an enhanced gas spin by a factor of $\lambda_{\text{gas}}/\lambda_{\text{dm}} \approx 1.3$ compared to the dark matter. This gain appears to arise from a transfer of specific angular momentum from dark matter to the gas during late-time halo assembly. This could be explained by infalling substructures getting their gas component ram pressure displaced, leading to a mutual torque between the dark matter and gas components allowing for a net transfer of specific angular momentum from dark matter onto gas. Such a transfer is also reflected in a small deficit of specific angular momentum at $z = 0$ in the dark matter component of the non-radiative simulation compared to the dark matter only simulation. The amount of specific angular momentum missing in the dark matter is exactly what is needed to balance the gain observed in the gas component.

In simulations with active galaxy formation physics the enhancement of the baryonic spin is even larger and leads to an average ratio of $\lambda_{\text{gas}}/\lambda_{\text{dm}} \approx 1.8$. We derive this value from a large sample of $\sim 320,000$ FOF-haloes from the *Illustris-1* simulation. If we assume that galactic winds and AGN feedback expel preferentially low specific angular momentum gas from a halo, we can estimate the expected apparent gain of specific angular momentum in the baryonic component based on the total baryonic mass lost from haloes. On average we find an expected enhancement by a factor of ~ 1.55 from this effect. Combining this with the relative enhancement of ~ 1.3 expected from the transfer of specific angular momentum from dark matter to the gas as seen in the non-radiative case, we arrive at a total enhancement by a factor of roughly ~ 2 relative to the dark matter spin. Note that this value represents a slight overestimate as our calculation does not take into account some of the low specific angular momentum being locked up in stars and remaining in the halo. However, the good agreement with the actually measured enhancement factor of ~ 1.8 shows that these two effects combined are sufficient to explain the higher specific angular momentum of the baryonic content

in the full physics simulations. This also casts doubts onto recent suggestions (Stewart et al. 2016) that cold filamentary gas accretion is responsible for the enhanced baryonic spin of haloes.

We also find that the different feedback mechanisms induce a strong dependence of the gas spin on halo mass. In low and high mass haloes, where galactic winds and AGN feedback are most efficient in expelling low specific angular momentum gas, the gas spin is highest. The stellar spin is far less affected, as star-formation takes place in cold, dense gas in the inner region of haloes, where the material is slowly rotating. The stellar component thus has small spin largely independent of halo mass. The baryonic spin is ultimately determined by the gas to stellar mass ratio of haloes which decreases with halo mass. Another consequence from feedback processes perturbing the gas component is a growing misalignment between the dark matter and gas component with cosmic time, which again is largest at halo masses that allow for most efficient feedback. Furthermore, we find that the alignment between the different halo components is a strong function of halo mass.

Our results thus clearly show that the baryonic spin sensitively depends on the galaxy formation physics employed. Highly schematic schemes for the evolution of the baryonic spin component, such as invoked in simple inside-out scenarios for disk formation that assume equal specific spin in dark matter and gas, need therefore be treated with caution. It will be interesting to examine with future simulations how strongly our results for the full physics simulations depend on the details of the feedback modelling invoked to regulate the galaxy formation process. Given the substantial impact of feedback one may be inclined to anticipate a very large range of possible outcomes. However, it appears also possible that the constraint to reproduce basic observational facts such as the galaxy stellar mass function effectively ties down the simulation predictions for the spin properties, independent of the specific realisation of the feedback physics.

ACKNOWLEDGMENTS

We thank the referee for insightful comments that helped to improve the paper. JZ and VS acknowledge financial support from the Deutsche Forschungsgemeinschaft through Transregio 33, “The Dark Universe”, and through the Klaus Tschira Foundation. VS also acknowledges support through the European Research Council under ERC-StG grant EXAGAL-308037. Some of the computations were performed on the HazelHen supercomputer at the High-Performance Computing Center Stuttgart (HLRS) as part of project GCS-ILLU of the Gauss Centre for Supercomputing (GCS). JZ acknowledges support from International Max-Planck Research School for Astronomy and Cosmic Physics at the University of Heidelberg (IMPRS-HD).

REFERENCES

- Avila-Reese V., Colín P., Gottlöber S., Firmani C., Maultsby C., 2005, *ApJ*, 634, 51
- Baldi A. S., De Petris M., Sembolini F., Yepes G., Lamagna L., Rasia E., 2016, *ArXiv e-prints*
- Barnes J., Efstathiou G., 1987, *ApJ*, 319, 575
- Bett P., Eke V., Frenk C. S., Jenkins A., Helly J., Navarro J., 2007, *MNRAS*, 376, 215
- Bett P., Eke V., Frenk C. S., Jenkins A., Okamoto T., 2010, *MNRAS*, 404, 1137
- Blumenthal G. R., Faber S. M., Primack J. R., Rees M. J., 1984, *Nature*, 311, 517
- Bryan G. L., Norman M. L., 1998, *ApJ*, 495, 80
- Bryan S. E., Kay S. T., Duffy A. R., Schaye J., Dalla Vecchia C., Booth C. M., 2013, *MNRAS*, 429, 3316
- Bullock J. S., Dekel A., Kolatt T. S., Kravtsov A. V., Klypin A. A., Porciani C., Primack J. R., 2001, *ApJ*, 555, 240
- Chen D. N., Jing Y. P., Yoshikawa K., 2003, *ApJ*, 597, 35
- Cole S., Lacey C., 1996, *MNRAS*, 281, 716
- Danovich M., Dekel A., Hahn O., Ceverino D., Primack J., 2015, *MNRAS*, 449, 2087
- Davis M., Efstathiou G., Frenk C. S., White S. D. M., 1985, *ApJ*, 292, 371
- Doroshkevich A. G., 1970, *Astrofizika*, 6, 581
- Dubois Y., Peirani S., Pichon C., Devriendt J., Gavazzi R., Welker C., Volonteri M., 2016, *ArXiv e-prints*
- Fall S. M., Efstathiou G., 1980, *MNRAS*, 193, 189
- Genel S., Fall S. M., Hernquist L., Vogelsberger M., Snyder G. F., Rodriguez-Gomez V., Sijacki D., Springel V., 2015, *ApJ*, 804, L40
- Gottlöber S., Yepes G., 2007, *ApJ*, 664, 117
- Hahn O., Teyssier R., Carollo C. M., 2010, *MNRAS*, 405, 274
- Heavens A., Peacock J., 1988, *MNRAS*, 232, 339
- Hoyle F., 1949, in *Problems of Cosmical Aerodynamics*, p. 195
- Macciò A. V., Dutton A. A., van den Bosch F. C., 2008, *MNRAS*, 391, 1940
- Macciò A. V., Dutton A. A., van den Bosch F. C., Moore B., Potter D., Stadel J., 2007, *MNRAS*, 378, 55
- Maller A. H., Dekel A., 2002, *MNRAS*, 335, 487
- Maller A. H., Dekel A., Somerville R., 2002, *MNRAS*, 329, 423
- Mo H. J., Mao S., White S. D. M., 1998, *MNRAS*, 295, 319
- Navarro J. F., Frenk C. S., White S. D. M., 1997, *ApJ*, 490, 493
- Nelson D. et al., 2015, *Astronomy and Computing*, 13, 12
- Neto A. F. et al., 2007, *MNRAS*, 381, 1450
- Okamoto T., Frenk C. S., Jenkins A., Theuns T., 2010, *MNRAS*, 406, 208
- Pakmor R., Springel V., Bauer A., Mocz P., Muñoz D. J., Ohlmann S. T., Schaal K., Zhu C., 2016, *MNRAS*, 455, 1134
- Peebles P. J. E., 1969, *ApJ*, 155, 393
- Rodriguez-Gomez V. et al., 2016, *ArXiv e-prints*
- Rubin V. C., Ford, Jr. W. K., 1970, *ApJ*, 159, 379
- Ryden B. S., 1988, *ApJ*, 329, 589
- Sales L. V., Navarro J. F., Theuns T., Schaye J., White S. D. M., Frenk C. S., Crain R. A., Dalla Vecchia C., 2012, *MNRAS*, 423, 1544
- Schäfer B. M., Merkel P. M., 2012, *MNRAS*, 421, 2751
- Schaye J. et al., 2015, *MNRAS*, 446, 521
- Shapiro P. R., Iliev I. T., Martel H., Ahn K., Alvarez M. A., 2004, *ArXiv Astrophysics e-prints*
- Sharma S., Steinmetz M., 2005, *ApJ*, 628, 21

- Sharma S., Steinmetz M., Bland-Hawthorn J., 2012, *ApJ*, 750, 107
- Springel V., 2010a, *MNRAS*, 401, 791
- Springel V., 2010b, *ARA&A*, 48, 391
- Springel V. et al., 2005, *Nature*, 435, 629
- Springel V., White S. D. M., Tormen G., Kauffmann G., 2001, *MNRAS*, 328, 726
- Steinmetz M., Bartelmann M., 1995, *MNRAS*, 272, 570
- Stewart K. et al., 2016, *ArXiv e-prints*, 1606.08542
- Teklu A. F., Remus R.-S., Dolag K., Beck A. M., Burkert A., Schmidt A. S., Schulze F., Steinborn L. K., 2015, *ApJ*, 812, 29
- van den Bosch F. C., 1998, *ApJ*, 507, 601
- van den Bosch F. C., Abel T., Croft R. A. C., Hernquist L., White S. D. M., 2002, *ApJ*, 576, 21
- Vitvitska M., Klypin A. A., Kravtsov A. V., Wechsler R. H., Primack J. R., Bullock J. S., 2002, *ApJ*, 581, 799
- Vogelsberger M., Genel S., Sijacki D., Torrey P., Springel V., Hernquist L., 2013, *MNRAS*, 436, 3031
- Vogelsberger M. et al., 2014, *Nature*, 509, 177
- Warren M. S., Quinn P. J., Salmon J. K., Zurek W. H., 1992, *ApJ*, 399, 405
- White S. D. M., 1984, *ApJ*, 286, 38
- White S. D. M., Rees M. J., 1978, *MNRAS*, 183, 341
- Zavala J. et al., 2016, *MNRAS*, 460, 4466
- Zavala J., Okamoto T., Frenk C. S., 2008, *MNRAS*, 387, 364

Name	description
GroupEkin	kinetic energy of FOF-haloes
GroupEthr	thermal energy of the gas component of FOF-haloes
GroupEpot	potential energy of FOF-haloes
Group_J	total angular momentum of FOF-haloes
Group_Jdm	angular momentum of the dark matter component of FOF-haloes
Group_Jgas	angular momentum of the gas component of FOF-haloes
Group_Jstars	angular momentum of the stellar component of FOF-haloes
Group_CMFrac	total counter-rotating mass fraction of FOF-haloes
Group_CMFracType	counter-rotating mass fractions per type: dark matter, gas, stars
Group_Ekin_*	kinetic energy of SO-haloes
Group_Ethr_*	thermal energy of the gas component of SO-haloes
Group_Epot_*	potential energy of SO-haloes
Group_J_*	total angular momentum of SO-haloes
Group_Jdm_*	angular momentum of the dark matter component of SO-haloes
Group_Jgas_*	angular momentum of the gas component of SO-haloes
Group_Jstars_*	angular momentum of the stellar component of SO-haloes
Group_CMFrac_*	total counter-rotating mass fraction of SO-haloes
Group_LenType_*	number of particles/cells of each matter type in SO-haloes
Group_MassType_*	mass per matter type in SO-haloes
Group_CMFracType_*	counter-rotating mass fractions per matter type in SO-haloes

Table A1. Full list of all newly available halo properties in the group catalogue extension. A halo can be either defined as a friends-of-friends (FOF) group or a spherical overdensity (SO). The latter can be either with respect to 200 times the critical density (Crit200), 500 times the critical density (Crit500), 200 times the mean density (Mean200), or with the redshift dependent overdensity expected for the generalised top-hat collapse model in a Λ -cosmology (TopHat200), see Bryan & Norman (1998). The corresponding properties can be accessed by replacing * with the terms in brackets. The different matter types in question are dark matter, gas, stars, and black holes.

Name	description
SubhaloEkin	kinetic energy of subhaloes
SubhaloEthr	thermal energy of the gas component of subhaloes
SubhaloEpot	potential energy of subhaloes
Subhalo_J(*)	total angular momentum of subhaloes
Subhalo_Jdm(*)	angular momentum of the dark matter component of subhaloes
Subhalo_Jgas(*)	angular momentum of the gas component of subhaloes
Subhalo_Jstars(*)	angular momentum of the stellar component of subhaloes
Subhalo_CMFrac(*)	total counter-rotating mass fraction of subhaloes
Subhalo_CMFracType(*)	counter-rotating mass fractions per type: dark matter, gas, stars

Table A2. Full list of all newly available galaxy properties in the group catalogue extension. Subhaloes corresponding to galaxies are defined as all particles/cells that are gravitationally bound the same potential minimum. Furthermore, we include two more definitions of a galaxy that are closer to the observational approach and include only subhalo particles/cells that are in the stellar half mass radius (InHalfRad) or twice the stellar half mass radius (InRad). The corresponding properties can be accessed by replacing * with the terms in brackets. The different matter types in question are dark matter, gas, stars, and black holes.

APPENDIX A: FIELDS OF EXTENDED GROUP CATALOGUE

For completeness and as a reference, we here provide a full list of all newly available halo and subhalo properties in the group catalogue extension we computed for *Illustris*. These additional properties will be made available as part of the public data release (Nelson et al. 2015) of *Illustris*.